Review

Invited

Methodology of Brain Perfusion Imaging

Emmanuel L. Barbier, PhD,[1,2] Laurent Lamalle, PhD,[1] and Michel Décorps, PhD[1]*

Numerous techniques have been proposed in the last 15 years to measure various perfusion-related parameters in the brain. In particular, two approaches have proven extremely successful: injection of paramagnetic contrast agents for measuring cerebral blood volumes (CBV) and arterial spin labeling (ASL) for measuring cerebral blood flows (CBF). This review presents the methodology of the different magnetic resonance imaging (MRI) techniques in use for CBV and CBF measurements and briefly discusses their limitations and potentials. J. Magn. Reson. Imaging 2001;13:496–520. © 2001 Wiley-Liss, Inc.

Index terms: cerebral blood volume; cerebral blood flow; mean transit time; transit time; magnetic resonance imaging; dynamic susceptibility contrast; contrast agent; bolus tracking; arterial spin labeling; arterial spin tagging; functional imaging; neuroimaging; review

MAGNETIC RESONANCE (MR) has been known for a long time to be one of the most powerful techniques to study coherent, as well as incoherent, motion. The effect of diffusion (incoherent motion) on the relaxation times and on the intensity of spin echoes has been discussed by Bloembergen et al (1) and by Hahn (2). The first report on flow (coherent motion) measurements using nuclear MR (NMR) dates back as far as 1951, when the first flow experiment using continuous wave was described by Suryan (3). Since these early studies, a number of review articles and book chapters on diffusion, perfusion, and flow measurements by NMR have been published (4–11).

MR imaging (MRI) now gives access to information on cerebral perfusion (12–22) that is of importance for the diagnosis and therapeutic follow-up of various brain pathologies. Many methods using endogenous or exogenous tracers have been developed in order to image various parameters related to perfusion. However, the relation between these parameters and the MR signal is complex. To understand the influence of blood on the MR signal is a key issue to derive accurate information about perfusion, either in healthy or in pathological conditions.

This review is mainly focused on the physical basis of the various phenomena involved in MR perfusion imaging and on the methodological description of the different techniques currently evaluated or in use. In each case, the quantification of the different parameters is discussed. Section 1 presents the perfusion parameters that are accessible with MR. In section 2, the contrast mechanisms involved when using blood pool agents are summarized. Such contrast-enhancing agents are used in bolus tracking techniques and in steady-state techniques, as discussed in sections 3 and 4, respectively. Section 5 describes the use of diffusible tracers and is centered on arterial spin-labeling (ASL) techniques.

SECTION 1: CEREBRAL PERFUSION: MEASURABLE PARAMETERS

Three important hemodynamic parameters are cerebral blood volume (CBV), cerebral blood flow (CBF), and mean transit time (MTT). The abbreviations rCBV, rCBF, and rMTT usually mean regional CBV, CBF, and MTT. However, the letter "r" can also indicate that the measurement is relative and not absolute (23). In the following, we shall use "r" for regional. The blood oxygenation level and the permeability of the blood-brain barrier (BBB) are also important physiological parameters relevant to the notion of brain perfusion. The MR methods available to measure these parameters are not in the scope of this review.

rCBV is defined as the volume of blood in a brain voxel divided by the mass of the voxel. Generally, rCBV involves only the microvasculature (i.e., arterioles, capillaries, and venules):

$$rCBV = \frac{\text{Volume of blood in a voxel}}{\text{Mass of the voxel}}. \qquad (1)$$

rCBV is frequently given in milliliters per 100 gram of tissue, or in microliters per gram ($\mu L\, g^{-1}$). rCBV can also be defined as a volume fraction:

$$rCBV\,(\%) = 100\,\frac{\text{Volume of blood in a voxel}}{\text{Volume of the voxel}}. \qquad (2)$$

Table 1
Typical Cerebral Blood Volume (CBV) Values, Obtained Using Non-NMR Methods

Tissue	Method	CBV
Human brain (242)	SPECT[a]	48.4 $\mu L\ g^{-1}$
Baboon (243)	PET[b]	31 $\mu L\ g^{-1}$
Rat brain (244), cortical parietal surface	Optical technique: bolus tracking	34 $\mu L\ g^{-1}$
Rat, whole brain (245)	Autoradiography	26.7 $\mu L\ g^{-1}$

[a]Single photon emission computed tomography.
[b]Positron emission tomography.

To convert between the two quantities, one can use the following relationship, which takes into account the mean density of brain tissue:

$$rCBV\ (\%) = 0.104\ rCBV\ (\mu L\ g^{-1}). \qquad (3)$$

The arteriolar, capillary, and venular volumes were reported to be approximately 21%, 33%, and 46% of the total microvascular blood volume, respectively (24).

The CBV may also be split into cerebral plasma volume (CPV) and cerebral red cell volume (CRCV):

$$CBV = CPV + CRCV. \qquad (4)$$

Non-NMR techniques to measure CPV and CRCV in humans and large animals include positron emission tomography (PET) and single photon emission computed tomography (SPECT) (25). These noninvasive methods are not readily applicable in vivo to small animals, for which perfusion measurement relies instead on the administration of a radioactive tracer and in vitro analysis. Typical values of CBV are summarized in Table 1.

rCBF is defined as the net blood flow through the voxel divided by the mass of the voxel:

$$rCBF = \frac{\text{Net blood flow through the voxel}}{\text{Mass of the voxel}}. \qquad (5)$$

Commonly used units for CBF are milliliters per 100 gram of tissue per minute and microliters per gram per second ($\mu L\ g^{-1}$ second^{-1}). Typical CBF values obtained from non-MR techniques are summarized in Table 2.

The rMTT describes the average amount of time it takes any water molecule or particle of contrast agent to pass through the voxel vasculature. rMTT is generally expressed in seconds and is given by

$$rMTT = \frac{rCBV}{rCBF}. \qquad (6)$$

Whereas CBF and MTT measurements necessarily rely on techniques sensitive to motion (for instance, bolus tracking techniques), CBV may be measured with other methods (for instance, in a steady state).

Many other physiological parameters intervene and complicate perfusion measurements. For instance, hematocrit (Hct), defined by the ratio

$$Hct\ (\%) = 100\ \frac{CRCV}{CBV}, \qquad (7)$$

is known to be smaller in the brain capillaries (Hct^{bc}) than in large vessels (Hct^{lv}). A mean ratio Hct^{bc}/Hct^{lv} of 0.83 was reported by Todd et al (26), whereas Bereckzi et al (27) found a mean ratio of about 0.60 in the rat gray matter. A capillary Hct of 30% and a venous Hct of 40% were recently considered for modeling the microvascular network (28). As discussed in sections 2–4, brain capillary Hct is a parameter that must be considered with many MR techniques using plasma markers.

Note that in sections 2–4, *tissue* is to be understood as including the extravascular and the microvascular compartments, with the exception of large vessels. This notion, in agreement with the literature related to blood pool contrast agents, is different from the definition adopted in section 5, where *tissue* excludes any vascular component, as generally found in the ASL literature.

The ultimate goal of MRI perfusion studies is the assessment of regional perfusion from MR image intensity. One can distinguish two MR approaches to detect and characterize the microvascular circulation. One approach involves the use of endogenous (24) or exogenous (13) blood pool tracers, that is, tracers that stay within the intravascular space (cf. sections 2–4). The other approach uses endogenous (29) or exogenous (30) diffusible tracers, which exchange between intra- and extravascular compartments, such as water (cf. section 5) (31).

SECTION 2: CONTRAST ENHANCEMENT WITH BLOOD POOL AGENTS: PHYSICAL BASIS

Although the amount of an adequately chosen intravascular tracer can be accessed directly using nonproton MR (32), we focus in the next sections (2–4) on the techniques for CBV, CBF, and MTT mapping that rely on the relaxation effects on the MR proton signal of

Table 2
Typical Cerebral Blood Flow (CBF) Values, Obtained Using Non-NMR Methods

Tissue	Method	CBF
Human brain (246), mean value over various brain areas	PET[a]	58 ml 100 g^{-1} min^{-1} (9.66 $\mu L\ g^{-1}\ s^{-1}$)
Baboon (243)	PET[a]	44 ml 100 g^{-1} min^{-1} (7.33 $\mu L\ g^{-1}\ s^{-1}$)
Rat brain (244), cortical parietal surface	Optical technique: bolus tracking	144 ml 100 g^{-1} min^{-1} (24 $\mu L\ g^{-1}\ s^{-1}$)
Rat, whole brain (245)	Autoradiography	101 ml 100 g^{-1} min^{-1} (16.8 $\mu L\ g^{-1}\ s^{-1}$)

[a]Positron emission tomography.

purely intravascular tracers. Recently, van Zijl et al reported CBV measurements using hemoglobin as an intravascular contrast agent (24,33). In the following (sections 2–4), we will only consider the most common approaches in which blood pool tracer perfusion imaging is carried out with exogenous paramagnetic contrast agents, such as gadolinium chelates or superparamagnetic iron oxide (SPIO) compounds (13,34).

A nondiffusible contrast agent does not cross the intact BBB and remains in the intravascular compartment, where it changes the blood T_1 and T_2. However, although the agent is confined to the vascular space, its effects extend to the extravascular space as well, due to magnetic susceptibility effects and to water exchange between blood and tissue. As a result, the presence of a nondiffusible contrast agent within the vascular bed may also change the relaxation times in the adjacent tissue.

In brain lesions (for example, in tumors), the BBB can be disrupted, resulting in the expansion of the distribution volume of the contrast agent from the intravascular space to the extravascular extracellular space. This may introduce errors in perfusion mapping (35,36).

Susceptibility

The magnetic field $\vec{B}$ in a sample depends both on the strength of the magnet and on the materials that make up the sample, as described by the formula:

$$\vec{B} = \vec{B}_0(1 + \chi), \qquad (8)$$

where χ is the magnetic susceptibility constant of the sample and $\vec{B}_0$ is the magnetic field in the absence of the sample. Tissue χ is very small and negative ($\chi = -10^{-5}$ to -10^{-6}). The magnetic field B in the tissue being smaller than B_0, is a diamagnetic substance. MRI contrast agents (34) are either paramagnetic (e.g., gadolinium-DTPA) or superparamagnetic (e.g., AMI 227), i.e., their χ is positive. The magnetic susceptibility of paramagnetic materials (such as deoxyhemoglobin, oxygen, or nitric oxide) ranges from 10^{-3} to 10^{-5}. With superparamagnetic materials, χ depends on the magnetic field strength. The increase in blood susceptibility induced by the contrast agent is proportional to the concentration of the latter in the blood pool.

Changes in Blood Relaxation Rates

The injection of a contrast agent in the blood pool changes the blood water relaxation rates. The change in blood water longitudinal relaxation rate may be easily obtained from the relaxivity r_1 and the blood concentration c_b of the contrast agent:

$$R_1 = R_1^0 + r_1 c_b, \qquad (9)$$

where $R_1 = 1/T_1$ and R_1^0 is the intrinsic blood water relaxation (all the symbols used in sections 2–4 are collected in Table 3). Note that since the contrast agent is a plasma marker, any local change in Hct results in a change in blood T_1. The linear relationship between the

blood water relaxation rate and the concentration of the contrast agent is at the basis of T_1-weighted perfusion imaging techniques.

The transverse relaxation of blood is predominantly due to diffusion of water protons through field gradients arising from the susceptibility difference $\Delta\chi_{RBC/plasma}$ between red blood cells (RBC) and plasma (28,37–40). $\Delta\chi_{RBC/plasma}$ can be written as

$$\Delta\chi_{RBC/plasma} = \chi_{RBC} - (\chi_{plasma} + \chi_{CA}), \qquad (10)$$

where χ_{RBC}, χ_{plasma}, and χ_{CA} are the volume susceptibilities of RBC, plasma, and the contrast agent, respectively. Since χ_{RBC} depends on the oxygenation level, $\Delta\chi_{RBC/plasma}$ and thus changes in the relaxation rate (ΔR_2) due to the injection of the contrast agent, also depend on the oxygenation level. For fully oxygenated blood, the injection of contrast agent increases $\Delta\chi_{RBC/plasma}$, resulting in a decreased blood T_2. With deoxygenated blood, the contrast agent injection may induce a decrease in $\Delta\chi_{RBC/plasma}$ and thus an increase in blood T_2.

Changes in T_1 in Adjacent Tissue

In the normal brain the BBB prevents diffusion of contrast agents out of the intravascular spaces. However, water exchange induces a change in extravascular T_1 (41). The residence time of water in capillaries has been considered to be on the order of 500 msec (42) (for discussion, cf. section 5, "Quantification of Blood Flow Using ASL Techniques"). Water exchange is slow (or possibly intermediate) with respect to MR measurement times, resulting in a limited shortening of tissue T_1 (41). It was shown that this effect of an intravascular MR contrast agent on the longitudinal relaxation time of the brain tissue could be used to simultaneously measure the permeability surface area product of water and the regional blood volume (43). However, the T_1 change is relatively small and the method has not found broad applications.

Changes in T_2 and T_2^* in Adjacent Tissue

The echo time in gradient-echo or spin-echo experiments is generally smaller than 100 msec, to be compared with a typical lifetime of water in capillaries probably on the order of 500 msec (42). Thus, here also water exchange between intra- and extravascular compartments is slow, and it does not contribute significantly to T_2 changes. The changes in tissue T_2 and T_2^* following the injection of an MR contrast agent are mainly due to the dephasing of the extravascular spins in the spatially nonuniform field created by the magnetic susceptibility differences ($\Delta\chi$) between vascular and extravascular compartments. This susceptibility difference causes magnetic field distortions in the vicinity of blood vessels, resulting in a decrease of the transverse relaxation times of protons in the extravascular compartment.

Thereby, the resonance frequency, which is proportional to the magnetic field, varies through the voxel: the presence of microscopic magnetic field heterogene-

Table 3
Parameters Used to Describe Non-Diffusible Tracer Methods

(r)CBV	Regional cerebral blood volume
(r)MTT	Regional mean transit time
(r)CBF	Regional cerebral blood flow
CPV	Cerebral plasma volume
CRCV	Cerebral red cells volume
Hct	Hematocrit
Hct^{bc}	Brain capillary hematocrit
Hct^{lv}	Large vessels hematocrit
r_1	Longitudinal relaxivity of the contrast agent
R_1^0	Intrinsic longitudinal relaxation rate of blood water
R_1	Intrinsic longitudinal relaxation rate of blood water (including contrast agent contribution)
$c_a(t)$	Arterial concentration of contrast agent[a]
$c_b(t)$	Blood concentration of contrast agent[a]
$C_t(t)$	Tissue concentration of contrast agent[a]
$\Re(t)$	Tissue concentration of contrast agent in response to an idealized bolus AIF[b]
$\Re^{Max}$	Peak height of $\Re(t)$
χ_{CA}^m	Molar susceptibility of contrast agent
χ_{CA}	Volume susceptibility of contrast agent
χ_{RBC}	Volume susceptibility of red blood cells
χ_{plasma}	Volume susceptibility of plasma
$\Delta\chi_{RBC/plasma}$	Susceptibility difference between red blood cells and plasma
l_D	Diffusion length
D	Self-diffusion coefficient of water
T_E	Echo time (either in spin-echo or in gradient-echo experiments)
S^{Pre}	Signal before contrast agent injection (steady-state technique)
S^{Post}	Signal after contrast agent injection (steady-state technique)
$S_{extra\ V}$	Extravascular contribution to the signal
$S_{intra\ V}$	Intravascular contribution to the signal
S_t	Tissue contribution to the signal

[a]Blood and tissue concentration of contrast agent do not have the same case since the tissue magnetization is expressed per g and the blood magnetization per ml.
[b]AIF, arterial input function.

ities creates a distribution of resonance frequencies. Two phenomena affect the transverse relaxation times in the presence of static field heterogeneities associated with the presence of a contrast agent in the blood pool (44–51). First, magnetic field perturbations increase the heterogeneity of the phase distribution across the voxel. Reversible spin dephasing occurs, with an associated signal loss in gradient-echo experiments and an increase ΔR_2^* in the relaxation rate $R_2^* = 1/T_2^*$. However, in the absence of diffusional motion, T_2, and thus $R_2 = 1/T_2$, remains unchanged (a spin-echo experiment refocuses the phase shifts due to a heterogeneous static field). Second, diffusion of water molecules in magnetic field gradients introduces two competitive effects:

(1) Irreversible losses of phase coherence and signal attenuation in spin-echo experiments;
(2) For rapid spatial variations of the magnetic field, possible averaging of phase differences by motional narrowing, resulting in reduced T_2^* and T_2 changes.

A salient implication of these effects is that changes in the transverse relaxation rates (ΔR_2 and ΔR_2^*) depend on the size and the architecture of the vascular compartment. A complete description of these phenomena can be found in references 44, 47, 49, 51, and 52.

Gradient-Echo Experiments: R_2^* Changes

At given rCBV, the change ΔR_2^* in R_2^* increases with vessel radius (r) and reaches a plateau (Fig. 1). For increasing $\Delta\chi$s (i.e., for increasing doses of contrast agent), the curve $\Delta R_2^*(r)$ is shifted to the left and the plateau is reached for lower vessel radii. At large doses of contrast agent, all the vascular components are on the plateau and gradient-echo experiments can measure the total vascular volume. It has been shown (47,51) that at the long echo times usually employed and at a high concentration of contrast agent, the enhancement in relaxation rate is given by

$$\Delta R_2^* = \frac{4}{3}\pi\gamma\chi_{CA}^m c_b B_0 \text{CBV}, \tag{11}$$

where CBV is the blood volume fraction (%) in the voxel of interest, χ_{CA}^m is the molar susceptibility of the contrast agent, and c_b is its blood concentration. Note that the product $c_b \times$ CBV represents here the contrast agent concentration in tissue.

In consequence, a gradient-echo technique is sensitive to both macro- and microvasculature (44). The linear relationship between ΔR_2^* and c_b is at the basis of perfusion imaging using dynamic susceptibility contrast (DSC) (cf. section 3). On the other hand, CBV may be obtained from the measurement of ΔR_2^* if $c_b\chi_{CA}^m$ is known: this result is at the basis of steady-state susceptibility contrast CBV imaging (cf. section 4).

Spin-Echo Experiments: R_2 Changes

In spin-echo experiments, the dephasing resulting from static local differences in Larmor frequencies is refo-
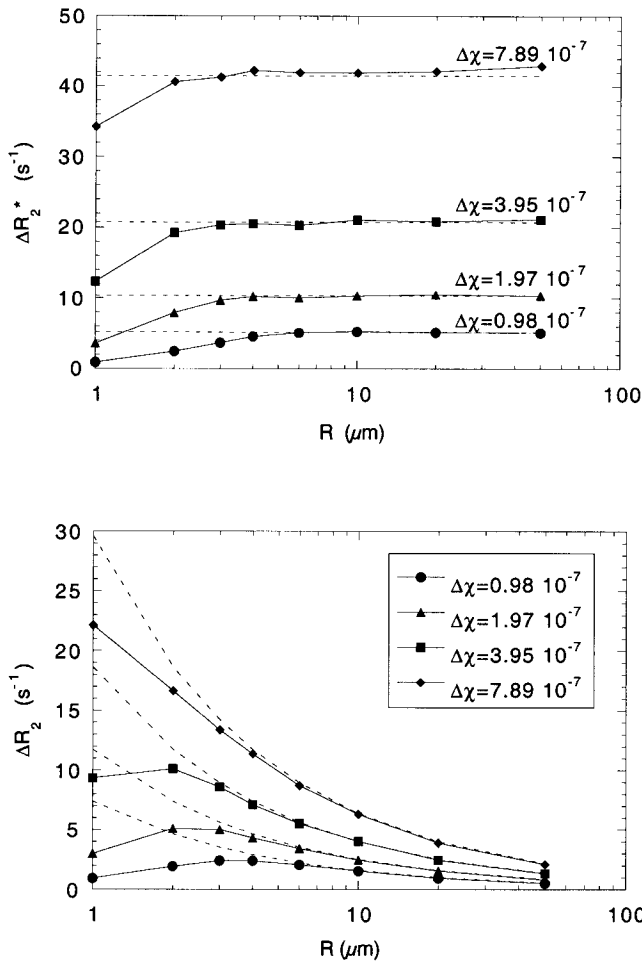
Figure 1. Results of Monte Carlo simulations showing, at 2.35 T and for a CBV of 2%, the effect of vessel radius (R) on the variation of the voxel reversible and irreversible relaxation rates (ΔR_2^* and ΔR_2) induced by the susceptibility difference between vascular and extravascular compartments. Each curve corresponds to a different susceptibility difference ($\Delta\chi$). The capillaries' radii range is typically 2–3 μm. (Courtesy of Irène Troprès and Stephan Grimault)

cused and diffusion effects become more visible. The phenomena that induce a change in transverse relaxation rates are closely related to the diffusion length during the experiment time T_E. This diffusion length L_D depends on the self-diffusion coefficient D of water in the vicinity of the vessel walls:

$$l_D = \sqrt{6DT_E} \; . \tag{12}$$

The water molecules move through field gradients induced by the blood-tissue susceptibility difference. With large vessels one can assume that during the experiment time (T_E) each diffusing water molecule experiences an approximately constant field gradient whose value depends on its initial position (slow diffusion approximation). Like with a Stejskal and Tanner sequence (53), an attenuation of the echo occurs (T_2 decrease). For small vessels, a diffusing water molecule experiences a whole range of magnetic fields resulting

in the averaging of phase differences (motional narrowing) and reduced signal attenuation.

At a given rCBV, the change in R_2 of a spin-echo experiment reaches a maximum for microvessels and decreases when vessel size increases (Fig. 1). For increasing $\Delta\chi$, the curve $\Delta R_2(r)$ shifts to the left. At $\Delta\chi \approx 0.4 \; 10^{-7}$, ΔR_2 peaks around the capillary radius (2–3 μm). Thus a spin-echo technique is mainly sensitive to microvasculature. This feature can be used to obtain information on the vascular architecture (54–57).

SECTION 3: BOLUS TRACKING TECHNIQUES

Basic Principles

While passing through the microvasculature, a bolus of contrast agent produces changes in the MR signal intensity. The change can be due either to susceptibility changes or to T_1 changes. The first works carried out in this area were based on the susceptibility effect (13,14). A linear relationship between the blood concentration of the contrast agent and the change in transverse relaxation rate is assumed (Eq. [11]). Further works were based on the T_1 effect (58). Whatever the source of contrast, the signal intensity-vs.-time curves are converted into concentration-vs.-time curves (Fig. 2). A gamma-variate function is then generally fitted to the latter to eliminate contribution of tracer recirculation (59).

Calculation of rCBV, rCBF, and rMTT from concentration-vs.-time curves is based on the indicator dilution methods for nondiffusible tracers (60,61). A bolus of nondiffusible tracer is given, resulting in a time-dependent arterial concentration of the contrast agent, $c_a(t)$, called arterial input function (AIF). CBV, CBF, and thus MTT (i.e. CBV/CBF) are obtained from measurement of both the AIF and the time dependence of the tracer concentration in the tissue, $C_t(t)$.
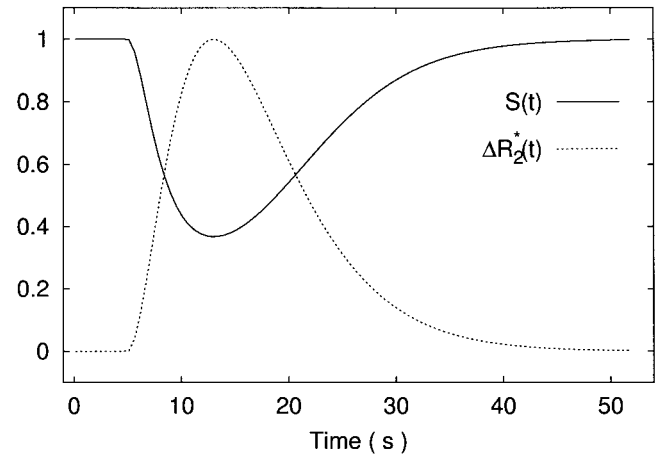
The CBV is given by (35,62):

Figure 2. Effect of the bolus on the MR signal intensity S(t) in a DSC experiment. The $\Delta R_2^*(t)$ curve, assumed to be proportional to that of the contrast agent concentration in tissue, is computed from S(t) according to Eq. [16].

$$CBV \propto \frac{\int_{-\infty}^{+\infty} C_t(t)dt}{\int_{-\infty}^{+\infty} c_a(t)dt}. \qquad (13)$$

Relative rCBV can be determined simply by measuring the area under the concentration-vs.-time curve (63), but absolute rCBV measurement requires the knowledge of the AIF.

The latter function can be estimated by measuring signal changes around or inside a major blood vessel. With experiments using plasmatic tracers, however, since local Hct varies with vessel diameter, the CBV value computed with Eq. [13] should be corrected by a factor $(1 - Hct^{iv})/(1 - Hct^{bc})$. Other phenomena, like partial volume effects and progressive spreading out of the bolus time shape for voxels further away from the location of the $c_a(t)$ measurement, also contribute to make difficult a correct determination of the AIF appropriate to the voxel.

The CBF could be computed from the peak height $CBF \times \Re^{Max}$ of the tissue concentration-vs.-time response $CBF \times \Re(t)$ to an idealized instantaneous bolus applied at t = 0 (35,62,64,65) according to

$$\frac{CBV}{CBF} = \frac{\int_{-\infty}^{+\infty} \Re(t)dt}{\Re^{Max}}. \qquad (14)$$

$\Re(t)$ represents the fraction of tracer still present in the tissue at time t after an ideal bolus injection. It decreases from $\Re(t) = 1$ to $\Re(\infty) = 0$. For a real bolus, however, the measured tissue concentration of contrast agent is the convolution product of $CBF \times \Re(t)$ with $c_a(t)$:

$$C_t(t) = \int_0^t CBF c_a(\tau)\Re(t - \tau)d\tau. \qquad (15)$$

To obtain CBF, one therefore needs to deconvolve the tissue concentration-vs.-time curve. This inverse problem remains a delicate one due to the difficult determination of the AIF and to the particular sensitivity of the deconvolution process to noise in the experimentally determined $C_t(t)$ and $c_a(t)$.

Several deconvolution approaches have been explored theoretically (35,66) and experimentally (36,64–66). $CBF \times \Re(t)$ can be determined either by fitting a shape predicted on the basis of a theoretical model for the vascular bed (parametric approach) or directly by the deconvolution process (nonparametric approach). Deconvolution itself can be performed either by Fourier transformation combined with Wiener filtering or algebraically by solving a discretized version of Eq. [15] with regularized least-squares methods. The nonparametric, model-independent approaches seem to provide more robust absolute rCBF estimates. In a recent study, $\Re(t)$ was determined iteratively with a maximum likelihood algorithm (66).

A correct determination of the concentration-vs.-time curves requires a high temporal resolution, and the development of dynamic bolus methods relies largely on the availability of fast T_1-, T_2-, and T_2*-weighted imaging techniques. With adequate preparation, many rapid acquisition schemes (gradient echo, keyhole, burst, EPI, spiral, presto, etc.) can be used. Because of its signal-to-noise ratio (SNR) advantage and of its time resolution, EPI is the reference method to monitor bolus injection (67). Due to its intrinsically low sensitivity to motion artifacts, spiral imaging could also be advantageous. For these two methods, an appropriate correction for artifacts induced by B_0 heterogeneity becomes particularly important for T_2* contrast. Note the recent introduction of a reversed spiral imaging scheme for increased T_2* contrast without TR lengthening (68). Whatever the selected technique, the parameters of the acquisition sequence must be carefully chosen (69–72), particularly to maximize the SNR.

Dynamic Susceptibility Contrast

Most of the published works on bolus tracking are based on the use of DSC (13,23,35,62,73–76). A T_2*-weighted imaging sequence is used to collect in each voxel the signal-vs.-time curve. The signal intensity is converted to a relative measure of the contrast agent concentration by the following relationship (Fig. 2):

$$C(t) = -\frac{k}{T_E} \ln\left(\frac{S(t)}{S(0)}\right), \qquad (16)$$

where T_E is the echo time and k is an unknown proportionality constant. To eliminate contribution of tracer recirculation, a gamma-variate function is generally fitted to the measured concentration-vs.-time curves. As mentioned above, for quantitative perfusion measurements, the AIF may be estimated from the signal of voxels containing or surrounding a large artery (36,62). CBV is then obtained with Eq. [13] and CBF with Eq. [15]. In addition to the problems previously described, one must be aware that it is difficult to measure the AIF with the same proportionality constant (k in Eq. [16]) as that for the tissue concentration-vs.-time curve. In brain tissue, the changes in R_2* during the first pass of contrast agent are due to extravascular spins, and the concentration of paramagnetic contrast agent is linearly related to the R_2* change for a small blood volume fraction (44). In blood, the R_2* change is due to the magnetic field gradients arising from the susceptibility difference between RBC and plasma (Eq. [10]), as well as to the R_2 relaxivity effect of the agent.

Moreover, obtaining C(t) from Eq. [16] is based on the assumption of the absence of any T_1 weighting, which suggests the use of a long TR, in contradiction with the requirement of a high temporal resolution. An alternative approach consists in acquiring multiple echoes to determine R_2*(t) maps from which ΔR_2*(t) can be computed as ΔR_2*(t) = R_2*(t) – R_2*(0), rather than by using Eq. [16] (66).

It should be noted that dynamic methods provide accurate measurements of the perfusion parameters only if the BBB is intact. A rupture of the BBB may introduce errors in CBV and CBF measurements. For moderate disruption of the BBB, a recently explored approach (77–79) to this problem consists in applying a model-based correction to the data to compensate for the tissue T_1 and T_2 variations arising from the contrast agent leakage to the extravascular space. The number of unknown parameters in the model is increased, however, and the acquisition protocol has to allow for both T_1 and T_2^* measurements, for instance with a multiple gradient-echo sequence (78,80,81). The use of large-size agents would allow a slower transport through the BBB (82), making possible perfusion measurements even in the case of damaged BBB.

Dynamic Relaxivity Contrast

Some first-pass bolus tracking techniques exploit T_1 changes (83–86), as measured by T_1-weighted acquisitions, to determine CBV (58). The method assumes that water exchange between the intra- and extravascular compartments is negligible and thus the MR signal can be written as:

$$S(t) = S_{\text{extra}V} + S_{\text{intra}V}(t). \qquad (17)$$

Assuming that $S_{\text{extra}V}$ is time independent, the change in signal can be written as

$$\Delta S(t) = S(t) - S(0) = S_{\text{intra}V}(t) - S_{\text{intra}V}(0) \qquad (18)$$

and originates from the blood only. Like with DSC, the signal intensity is converted to a relative concentration of the contrast agent. The change $\Delta R_1 = R_1^{\text{Post}} - R_1^{\text{Pre}}$ in the relaxation rate is linearly related to the blood concentration in the contrast agent (Eq. [9]).

With inversion-recovery or saturation-recovery fast imaging techniques, the image signal intensity is linearly related to R_1 for long T_1. At low T_1 values, which may be encountered at peak concentration, the slope of the signal-vs.-concentration relationship decreases (signal saturation). Alternatively, the contrast agent concentration can be obtained by using the analytical form of the signal-vs.-relaxation rate relationship. Determination of the AIF with the same proportionality constant than the tissue concentration-vs.-time curve might be easier with relaxivity contrast as with susceptibility contrast.

Applications of Bolus Tracking Techniques

For comparison of interindividual measurements, absolute CBV, MTT, and CBF values are highly desirable. Absolute quantification of CBV, MTT, and CBF, however, clearly remains a difficult problem and still asks for methodological improvements before to become routinely applicable. Nevertheless, if only through the determination of relative values (which permit, for instance, comparison of ipsi- and controlateral measurements), bolus tracking techniques have already been applied in fundamental biological studies (87) and in functional studies (88), progressively enter the clinical

practice (85,89–93). Clinical applications include the characterization of tumor vascularity (78,85,94), the follow-up of cancer treatments (95,96), the study of the vasodilatory capacity of brain during cerebral perturbations (76), the study of ischemia-reperfusion injuries (75) and stroke (84,97–99).

Often, DSC measurements are processed according to the following practical scheme. From the time series of acquired data, $\Delta R_2^*(t)$ curves can be computed that are assumed proportional to $C_t(t)$. After fitting a gamma-variate function and in the hypothesis of a constant AIF to the entire slice, an index of relative rCBV can be computed according to

$$\text{rCBV}_{\text{index}} = \int_0^t \Delta R_2^*(\tau)d\tau. \qquad (19)$$

In a pragmatic approach (100), without knowledge of the AIF, an rMTT index can be computed using the nondeconvolved $\Delta R_2^*(t)$ curve:

$$\text{rMTT}_{\text{index}} = \frac{\int_0^t \tau\Delta R_2^*(\tau)d\tau}{\int_0^t \Delta R_2^*(\tau)d\tau}. \qquad (20)$$

From these values, there results an rCBF index:

$$\text{rCBF}_{\text{index}} = \frac{\text{rCBV}_{\text{index}}}{\text{rMTT}_{\text{index}}}. \qquad (21)$$

Maps of these indices are presented in Fig. 3 for an ischemic edema-bearing patient. Weisskoff et al have shown that, although the first moment $\text{rMTT}_{\text{index}}$ computed directly from the $\Delta R_2^*(t)$ curve is not equal to CBV/CBF, it can still give a reasonably correct relative measurement of rCBF between regions, provided, however, that they feature a similar vascular physiology. This can also be used to continuously monitor the effect of a perturbation on a given region (100).

Some caution is required in the analysis of the perfusion index maps computed with Eqs. [19–21]. For a given AIF, a decrease in rCBF will affect the $\Delta R_2^*(t)$ curve by spreading it out, while its integral remains constant. In practice, this implies a lower SNR and, due to the limited observation window, a risk of truncature in the observed $\Delta R_2^*(t)$ (Fig. 4), degrading the accuracy of the computed integral. It is thus difficult to know whether a low $\text{rCBV}_{\text{index}}$ really indicates a region with low relative rCBV or with low rCBF, or both (Fig. 3–4).

Regarding relaxivity bolus tracking, Hackländer et al (85) have recently compared CBVs as determined by T_1 and T_2^* dynamic measurements. They found that the T_1 approach led to better quantification, but they also found that the T_2^* approach could provide faster acquisitions over multiple slices, a significant advantage from a clinical perspective. In a more recent study, Moody et al (101) compared CBV and CBF as obtained with the T_1 bolus tracking technique to SPECT mea-
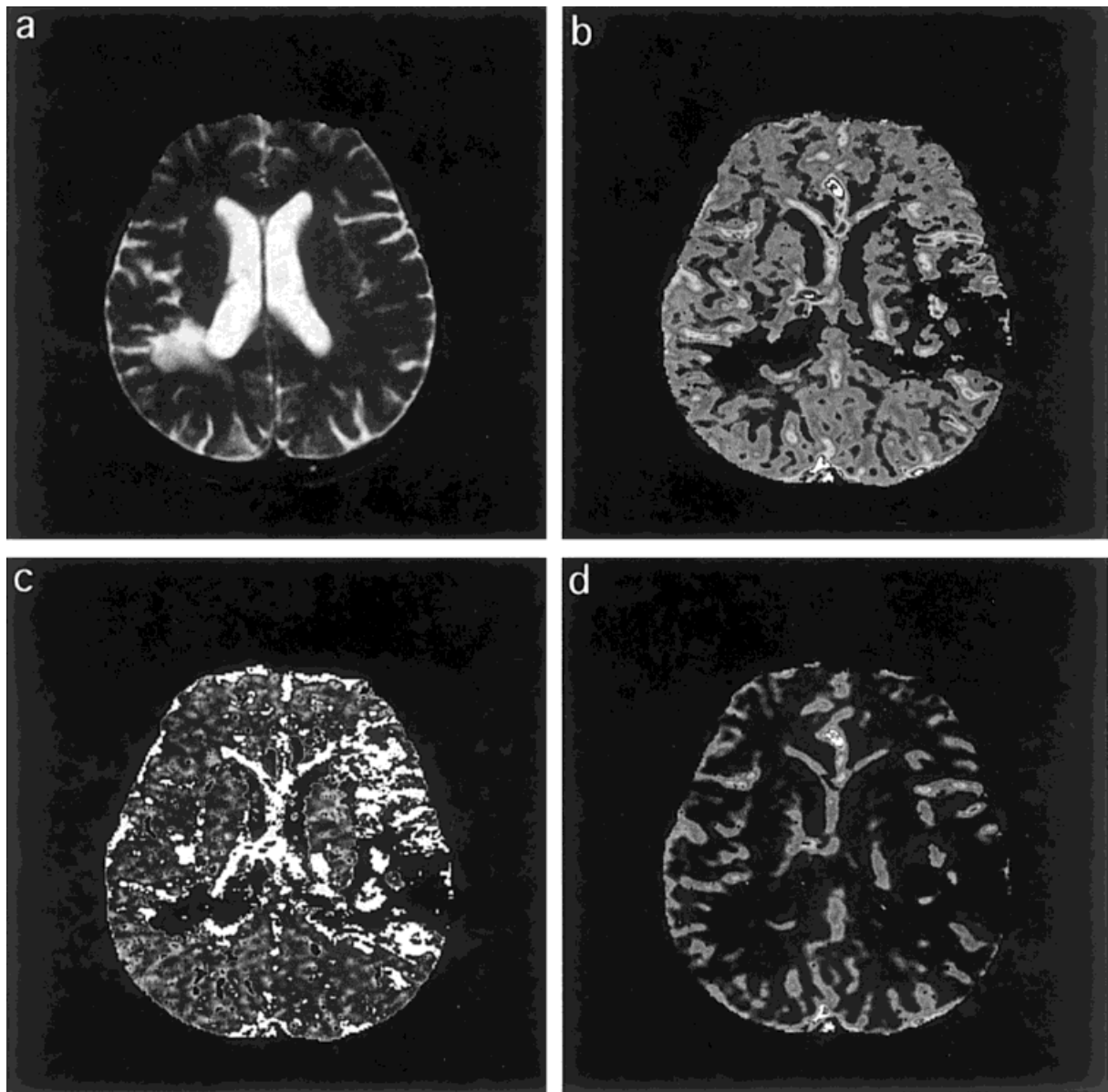
Figure 3. Anatomic, T_2-weighted image of an ischemic edema-bearing patient (**a**) and corresponding maps of the relative rCBV index (**b**), rMTT index (**c**), and rCBF index (**d**) computed from DSC data. Examples of $\Delta R_2^*(t)$ curves are given in Fig. 4. (Courtesy of Unité INSERM 438 and Unité IRM, CHU Michallon, Grenoble, France)

surements. In repeated measurements, they found a good reproducibility for the relative values.

SECTION 4: STEADY-STATE TECHNIQUES

With cerebral dynamic perfusion imaging in humans, the duration of the first passage of the bolus is approximately 5–20 seconds. The high temporal resolution required to determine rCBV and rCBF is obtained at the expense of spatial resolution and/or SNR. Another approach to rCBV (but not rCBF) mapping is steady-state contrast-enhanced MRI, which uses contrast agents with a long half-life in the vascular pool, such as ultrasmall SPIO (USPIO) ones, like AMI-227 (102). Like with dynamic methods, either relaxivity contrast (103–105) or susceptibility contrast (106–108) may be used (109,110). Steady-state techniques may be carried out with standard gradi-

ent-echo or spin-echo imaging sequences and allow continuous changes in relative rCBV to be monitored. Compared to dynamic techniques, steady-state perfusion MRI offers the advantage of a higher spatial resolution but does not allow rCBF and rMTT to be measured.

Steady-State Susceptibility Contrast

CBV imaging using steady-state susceptibility contrast exploits the linear relationship between the blood concentration of the contrast agent and the changes in R_2^* it induces (Eq. [11]). In many studies (28,54,56,107,111), the R_2^* changes induced by the contrast agent were obtained with a two-point technique, i.e., from the ratio of the signal intensities measured, at time T_E, before (S^{Pre}) and after (S^{Post}) contrast agent injection:
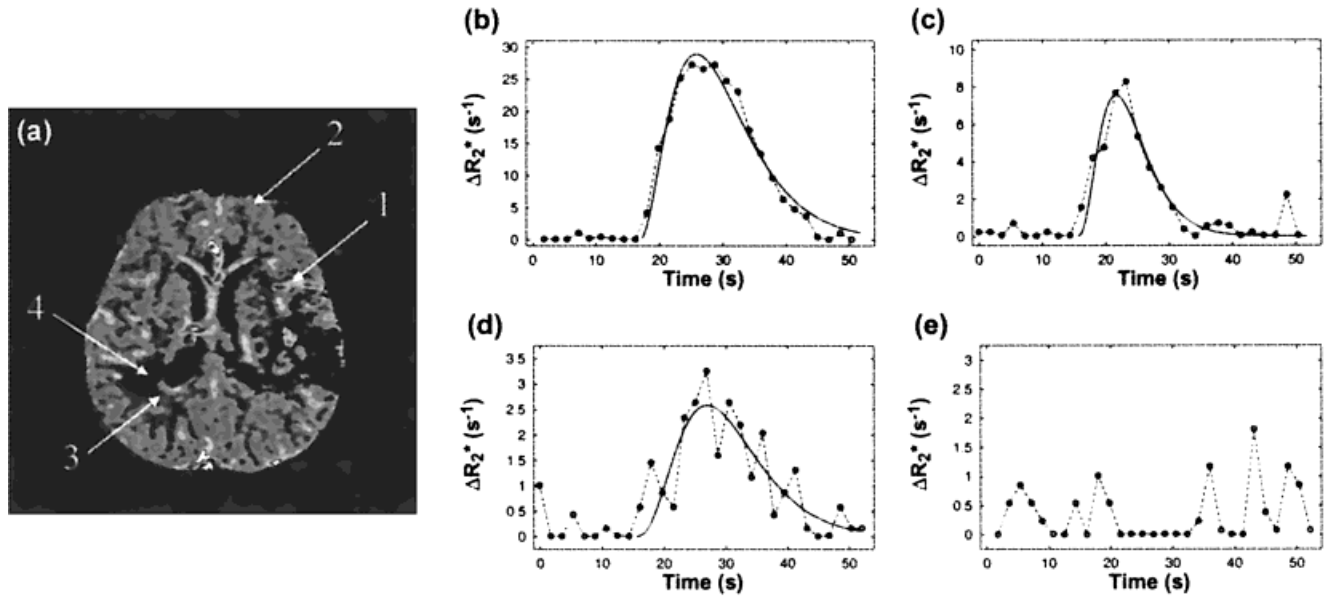
Figure 4. a: rCBV$_{index}$ map as in Fig. 3. **b–e:** Susceptibility bolus tracking curves obtained from the regions (1–4) pointed to by arrows in a. The variation of R$_2$*, consequential to the contrast agent bolus, is represented together with the fitted gamma-variate curves. Note the different vertical scales. In b, the observed voxel (arrow 1 in a) is close to a vessel and gives a high SNR in the ΔR$_2$*(t) curve. The voxel in c (arrow 2 in a) is at the periphery of an ischemic edema, and it is not clear whether to attribute the decreased intensity to a reduced CBF or to a lower relative CBV. In d, at the periphery of the lesion (arrow 3 in a), the decrease is more pronounced and the SNR becomes too low to permit an accurate estimation of the ΔR$_2$*(t) integral. Note the apparent truncation of the curve. The fact that the bolus is not seen in e, within the lesion (arrow 4 in a), may not be interpreted as revealing an absence of any flow, due to the degraded SNR. (Courtesy of Unité INSERM 438 and Unité IRM, CHU Michallon, Grenoble, France)

$$\Delta R_2^* = -\frac{1}{T_E} \ln\left(\frac{S^{Post}}{S^{Pre}}\right). \quad (22)$$

Due to the change in the cerebral tissue T$_1$ after injection (43), any T$_1$ weighting of the signal may introduce T$_E$-dependent errors. It is easy to show that a T$_1$ effect leads to an underestimation of ΔR$_2$* changes. Alternatively, a multiple gradient-echo sequence (55,109,112,113) can be used. Then R$_2$* is determined before and after contrast agent injection by least-squares fitting of the gradient-echo signal decay S(T$_E$) to a mono-exponential function. ΔR$_2$* maps are computed according to

$$\Delta R_2^* = \frac{1}{T_2^{*Post}} - \frac{1}{T_2^{*Pre}}, \quad (23)$$

where T$_2$*^{Pre} and T$_2$*^{Post} are the pre- and postinjection relaxation times. One advantage of this technique is its insensitivity to T$_1$ weighting.

Absolute rCBV can be obtained if the increase in the blood tissue susceptibility difference due to the injection of the contrast agent, $\Delta\chi = \chi_{CA}^m c_b$, is known.

Several factors might limit the accuracy of the CBV measurement using susceptibility contrast imaging. First, absolute measurement of CBV from ΔR$_2$* and Δχ is based on a very simplified model of the brain vessel architecture (47). Results obtained with this model, based on the static approximation (diffusion of tissue protons is not considered), however, were found to be in close agreement with Monte Carlo simulations (51).

Equation [11] has been successfully used even with low susceptibility differences (54,111,114,115). A second factor is the decrease of Hct as vessel size decreases. Since Δχ can be vessel-size dependent, the effective Δχ value may be inaccurately known. Third, the BBB should not be disrupted. Qualitative information on microvasculature can be obtained from R$_2$ changes by using a spin-echo sequence (116).

Steady-State Relaxivity Contrast

The determination of absolute rCBV with susceptibility contrast requires the knowledge of the proportionality constant between ΔR$_2$* and rCBV. As explained below, quantitative rCBV maps can be obtained with steady-state relaxivity contrast without prior knowledge of the blood concentration in the contrast agent.

Like with dynamic relaxivity contrast, it is assumed that the brain contains two separate, extravascular and intravascular, compartments. The signal before injection may then be written as

$$S_t = S_{extraV} + S_{intraV}. \quad (24)$$

If the water exchange between intra- and extravascular compartments is negligible, the tissue signal, S_t, remains unchanged after contrast agent injection. In this case, the increase in signal in the brain parenchyma due to contrast agent injection may be written as

$$\Delta S_t = \Delta S_{intraV}. \quad (25)$$

This increase in signal is related by

$$rCBV\ (\%) = 100\ \frac{\Delta S_{intraV}}{\Delta S_{ref}} \qquad (26)$$

to the signal increase ΔS_{ref} in a voxel that contains only blood.

The T_1 techniques require the measurement of the signal change in a large vessel. Partial volume effects, as well as differences in the Hct between capillaries and large draining veins, may then introduce errors in rCBV estimations. T_1 techniques could also suffer from the large, Hct-dependent change in blood T_2 due to the presence of the contrast agent in the blood compartment. A short echo time is thus required.

This class of techniques was based on a two-compartment model, and water exchange between the two compartments was neglected. When exchange is taken into account, it has been shown that an intravascular MR contrast agent changes the longitudinal relaxation time of the brain tissue (41,43). The T_1 change in the extravascular compartment due to water exchange is, however, limited and the change of S_t due to the contrast agent injection remains relatively small.

Applications of Steady-State Techniques

Despite the SNR and spatial resolution advantages of steady-state techniques, fewer studies using this approach have been published than studies using the dynamic method. This can be explained by the relatively recent introduction of contrast agents with a sufficiently long half-life in blood (117). Moreover, the examination times associated with steady-state methods are somewhat longer than with dynamic techniques, which is a disadvantage in a clinical context.

On animal models, however, this approach has already found several interesting applications. It has been applied for instance to better understand the blood oxygen level-dependent (BOLD) contrast observed in situations where changes in CBV and in oxygen saturation occur simultaneously, like with acute hypercapnia (111). Steady-state measurements of R_2 and R_2* can be used to measure CBV in tumors and to characterize quantitatively the distribution of vessel sizes in cerebral glioma (55,116). The vasodilatory capacity of the brain during cerebral perturbations has been evaluated using relaxivity, as well as susceptibility steady-state contrasts (103,109,113). Hamberg et al have measured CBV continuously during transient global ischemia followed by hyperemia using steady-state susceptibility contrast (106). In a study of injury subsequent to ischemia reperfusion, Quast et al (87) combined a steady-state spin-echo acquisition and a DSC acquisition to determine CBV and CBF, respectively. Recently, Zaharchuk et al (118,119) used ASL and steady-state susceptibility contrast to measure CBV, CBF, and BOLD signal changes during hemorrhagic hypotension in the rat.

SECTION 5: PERFUSION IMAGING: USE OF DIFFUSIBLE TRACERS

Physical Basis

Before the introduction of spin-labeling techniques, most MR approaches to characterize blood flow with diffusible tracers were derived from the experience acquired with freely diffusible radioactive tracers like ^{14}C-iodoantypirine (120,121), ^{133}Xe (122–124), or H_2^{15}O (125–128). Most of the radionucleides encountered in biology have isotopes with nonzero magnetic moment, which have been, not surprisingly, exploited in MR counterparts of the radioactive approach to measure rCBF. This is, for instance, the case of ^{2}H, ^{17}O, ^{19}F, and ^{1}H.

Besides ^{1}H, the natural abundance of all the other nuclei make the MR experiment very similar to the methods based on radioactivity, as the amount of signal detected is directly related to the amount of tracer in the tissue. Blood flow quantification is then generally based on the clearance approach, initially proposed by Kety and Schmidt (129). The amount of tracer in brain tissue depends on the inflowing (arterial) and outflowing (venous) amounts:

$$\frac{dC_t(t)}{dt} = rCBF[c_a(t) - c_v(t)]. \qquad (27)$$

Since the tracer is assumed to be freely diffusible, its tissue and venous concentrations must be equal after accounting for the molecular partition coefficient between blood and tissue, λ: $c_v(t) = C_t(t)/\lambda$. Equation [27] can be integrated between t = 0 (tracer arrival) and t = T (measurement time) (129):

$$C_t(T) = rCBF\ e^{-\,rCBF\ T/\lambda} \int_0^T c_a(t)e^{rCBF\ t/\lambda}dt. \qquad (28)$$

If the tracer arrives as an ideal bolus, then its clearance rate becomes:

$$C_t(T) = c_a(0)rCBF\ e^{-rCBF\ T/\lambda}. \qquad (29)$$

On that basis, Ackerman et al used ^2H_2O to quantify blood flow in the liver (130); subsequently, rCBF has been measured in various animals (131–134). Corbett et al compared such deuterium-based measurements to microsphere-based measurements in the piglet brain and reported an underestimation of rCBF for large blood flow values (134). This is probably due to limited diffusion of water in brain tissue (cf. section 5, "Quantification of Blood Flow Using ASL Techniques").

^{19}F is NMR detectable and can be easily incorporated in numerous volatile (and therefore inhalable) compounds, which make good tracers for perfusion. Eleff et al observed the clearance of freon-23 (or CHF_3) (135). Other volatile compounds containing ^{19}F were used to characterize rCBF, like halothane in a rat study (136) or freon-22 in a cat study (137). However, freon-23 has the least physiological effects (138). More recently, Pekar et al obtained a 0.4-cc resolution in the cat brain using

$CH^{19}F_3$ (139). The comparison with measurements based on microspheres showed that the use of freon-23 yielded an underestimation of rCBF, most certainly due to the limited diffusion of freon-23 in the brain tissue (140).

At about the same time, based on the pioneering work of Mateescu et al (141), $H_2^{17}O$ was also imaged directly to characterize rCBF (142,143). However, the natural abundance of $H_2^{17}O$ is not negligible (20.3 mMol (143)), and the clearance equation must be corrected for the effect of oxygen metabolism (143–145). $H_2^{17}O$ also has a well-known effect on proton T_2 (146,147). Kwong et al used the proton T_2 reduction induced by the passage of an intra-arterial bolus of ^{17}O-labeled water to map rCBF in dogs (148). Recently, Arai et al proposed a new strategy for in vivo autoradiography: the ^{17}O concentration is measured in the carotid by ^{17}O spectroscopy and the T_2 effect of $H_2^{17}O$ is detected in the brain by proton MR (149). Like all techniques based on water, the CBF quantification with $H_2^{17}O$ also suffers from diffusion limitation (cf. section 5, "Quantification of Blood Flow Using ASL Techniques").

As a final example of nonproton MR, Swanson et al recently mapped the distribution of ^{129}Xe in the brain (150). This is the first step toward rCBF measurements using hyperpolarized gases.

However, because water is endogenous and abundant, and because its technical implementation is far easier than that for the previously mentioned methods, the approach that is predominantly used to map rCBF is ASL.

Basic Principles of ASL

A modification of the state of blood magnetization in an artery—the labeling of arterial spins—induces a measurable change downstream in the apparent tissue T_1 and in the tissue magnetization. Both changes can be used to quantify blood flow (29,151).

As the labeled water flows into the tissue vasculature, water exchange between blood and tissue occurs through the BBB, yielding a magnetization exchange. These aspects make the ASL experiment very close to other magnetization transfer experiments, like the one described by Wolff and Balaban (152).

The general principles of ASL were first demonstrated by Detre et al and Kwong et al (29,151). Detre et al applied a sequence of saturation pulses on the rat neck and detected the resulting signal change in the brain (29). A distal saturation applied equidistantly outside the brain served as a control for the effects of saturation pulses on the magnetization of tissue macromolecules. Based on the fact that the apparent tissue T_1 changes with blood flow (29,31), Kwong et al used a train of inversion-recovery sequences to map rCBF variations during primary sensory stimulation (151). From the first papers describing the principles of blood flow measurement using ASL, a large diversity of schemes—and acronyms—has been proposed. Although there is no clear consensus on how to call each scheme (for instance, ASL is equally often called arterial spin tagging), the existing methods are generally divided into two groups, depending on how the blood is labeled, as re-

cently reviewed by Calamante et al (153): the continuous ASL methods (CASL) and the pulsed ASL methods (PASL).

Both the continuous and the pulsed ASL methods are based on the following principles. The arrival of labeled blood at the perfusion site is assumed to occur via uniform plugged flow (154). One defines the transit time τ as the time it takes for the labeled spins to go from the labeling plane to the perfusion site. In the imaged slice, the evolution of the tissue magnetization can be described by the following modified Bloch equation (29):

$$\frac{dM_t(t)}{dt} = \frac{M_t^0 - M_t(t)}{T_{1t}} + \text{rCBF}[m_a(t) - m_v(t)] \quad (30)$$

where the parameters are described in Table 4, as are all the other parameters used in section 5. At equilibrium, the relation between blood and tissue magnetizations involves the blood-brain partition coefficient, λ, which represents the difference between water concentrations in blood and in tissue (129,155,156):

$$m_a^0 = m_v^0 = \frac{M_t^0}{\lambda}. \quad (31)$$

Therefore, if arterial spins are not labeled upstream, one has

$$m_a(t) = m_a^0 = \frac{M_t^0}{\lambda}. \quad (32)$$

Detre et al assumed a full exchange between blood and tissue water and therefore considered the venous magnetization to be equal to the tissue magnetization:

$$m_v(t) = \frac{M_t(t)}{\lambda}. \quad (33)$$

Assuming that a slice-selective inversion pulse has been applied at t = 0 on the tissue magnetization, Eq. [30] yields

$$M_t(t) = M_t^0[1 - 2 \exp(-t/T_{1t,\text{app}})], \quad (34)$$

where $T_{1t,\text{app}}$, the apparent tissue T_1, is defined by

$$T_{1t,\text{app}} = \left(\frac{1}{T_{1t}} + \frac{\text{rCBF}}{\lambda}\right)^{-1}. \quad (35)$$

The fact that $T_{1t,\text{app}}$ depends on blood flow has been verified in the isolated perfused heart by Williams et al (157). This constitutes the basis of all ASL techniques, pulsed or continuous. After the arterial magnetization has been continuously saturated upstream ($m_a(t) = 0$), and provided it has been irrigating the tissue for a long period of time, the tissue magnetization reaches a steady state, M_t^{lab}. In this case, Detre et al showed that rCBF could be estimated with (29)

$$\text{rCBF} = \frac{\lambda}{T_{1t,\text{app}}} \left(1 - \frac{M_t^{\text{lab}}}{M_t^0}\right). \quad (36)$$

Table 4
Parameters Used to Described Diffusible Tracer Methods

$\alpha(t)$ and α_0	Degree of labeling at the arterial plane as a function of time and maximum degree of labeling at the arterial plane
$c_a(t)$	Arterial concentration of contrast agent[a]
$c_v(t)$	Venous concentration of contrast agent[a]
$C_t(t)$	Tissue concentration of contrast agent[a]
δ	Effect of water exchange between free protons and macromolecular protons in tissue on T_{1t}, in s^{-1}
E	Extraction fraction of the blood magnetization by the brain tissue (blood flow dependent)
(r)CBF	regional cerebral blood flow, in $ml \cdot g^{-1} \cdot s^{-1}$
k_{for} and k_{rev}	Magnetization transfer rate constant between free and macromolecular tissue protons
λ	Blood-brain water partition coefficient, in $ml \cdot g^{-1}$
$m_a(t)$ and m_a^0	Arterial magnetization per ml of blood, as a function of time and its equilibrium value[a]
$M_m(t)$ and M_m^0	Macromolecule magnetization per g of tissue, as a function of time and its equilibrium value[a]
$M_t(t)$ and M_t^0	Tissue magnetization per g of tissue, as a function of time and its equilibrium value[a]
$m_v(t)$ and m_v^0	Venous magnetization per ml of blood, as a function of time and at its equilibrium value[a]
T_{1a}	Spin-lattice relaxation time constant of free arterial protons, in the absence of cross relaxation with macromolecular protons, in s
T_{1m}	Spin-lattice relaxation time constant of macromolecular tissue protons, in the absence of cross relaxation with free protons, in s
T_{1t}	Spin-lattice relaxation time constant of free tissue protons, in the absence of cross relaxation with macromolecular protons and in the absence of blood flow, in s
$T_{1t,app}$	Spin-lattice relaxation time constant of free tissue protons, in the absence of cross relaxation with macromolecular protons but in presence of blood flow, in s
$T_{1t,sat}$	Spin-lattice relaxation time constant of free tissue protons, in presence of cross relaxation with macromolecular protons but in the absence of blood flow, in s
TI	Inversion delay, in s

[a]Blood and tissue magnetization (or concentration of contrast agent) do not have the same case since the tissue magnetization is expressed per g and the blood magnetization per ml.

Continuous ASL (CASL)

Flow-Driven Adiabatic Inversion

With CASL techniques, the blood magnetization is continuously labeled upstream, so that the measured tissue magnetization is in a steady state. By comparing the tissue magnetization in the normal condition (i.e., control state) and the tissue magnetization when it has been perfused by labeled blood (i.e., label state), one can estimate the blood flow. In order to achieve this continuous labeling, Detre et al first suggested using trains of saturation pulses (29). Shortly after, Williams et al proposed to replace using trains of saturation pulses by a flow-driven adiabatic inversion scheme (31), previously used by Dixon et al for angiography (158) (Fig. 5a). An adiabatic fast-passage inversion (159) is realized by continuously applying a low-power radiofrequency field in the presence of a magnetic field gradient aligned with the flow direction (31). A continuous inversion of arterial spins produces a tissue signal change two times larger than a continuous saturation. The degree of labeling, α_0, describes the efficiency of the spin labeling:

$$\alpha_0 = \frac{m_a^0 - m_a}{2m_a^0}. \tag{37}$$

Theoretically, for continuous saturation $\alpha_0 = 0.5$ and for continuous inversion $\alpha_0 = 1.0$. Zhang et al determined α_0 in vivo by imaging the large arteries downstream the labeling plane using a flow-compensated imaging technique (160). Due to the longitudinal relaxation that occurs during the transit time from the labeling plane to the perfusion site, the inversion state of the labeled spins at the perfusion site is no longer α_0, but becomes (161):

$$\alpha(\tau) = \alpha_0 \exp(-\tau/T_{1a}). \tag{38}$$

The efficiency of the velocity-driven adiabatic inversion has been theoretically and experimentally investigated by Maccota et al (162) and Marro et al (163). Maccota et al showed that, assuming a laminar flow, a degree of labeling of greater than 0.9 could easily be obtained over a broad range of flow velocities (from ~15 to ~150 cm · second^{-1}). They also indicated that the method proposed by Zhang et al to measure the degree of labeling was biased toward the lower range of laminar flow velocities.

One-Coil CASL

In the CASL experiment, the most general equation that describes the evolution of the tissue magnetization is the one accounting for both free and macromolecular protons (164–166):

$$\begin{cases} \dfrac{dM_t(t)}{dt} = \dfrac{M_t^0 - M_t(t)}{T_{1t}} - k_{for}M_t(t) + k_{rev}M_m(t) \\ \qquad\qquad + rCBF\, E[m_a(t) - m_v(t)] \\ \dfrac{dM_m(t)}{dt} = \dfrac{M_m^0 - M_m(t)}{T_{1m}} + k_{for}M_t(t) - k_{rev}M_m(t) \end{cases} \tag{39}$$

At equilibrium, free and macromolecular tissue magnetizations are related by

$$k_{\text{for}}M_t^0 = k_{\text{rev}}M_m^0. \qquad (40)$$

The model is illustrated in Fig. 6 (166). When the same coil is used for labeling and for imaging, the labeling pulse, applied off-resonance with respect to the
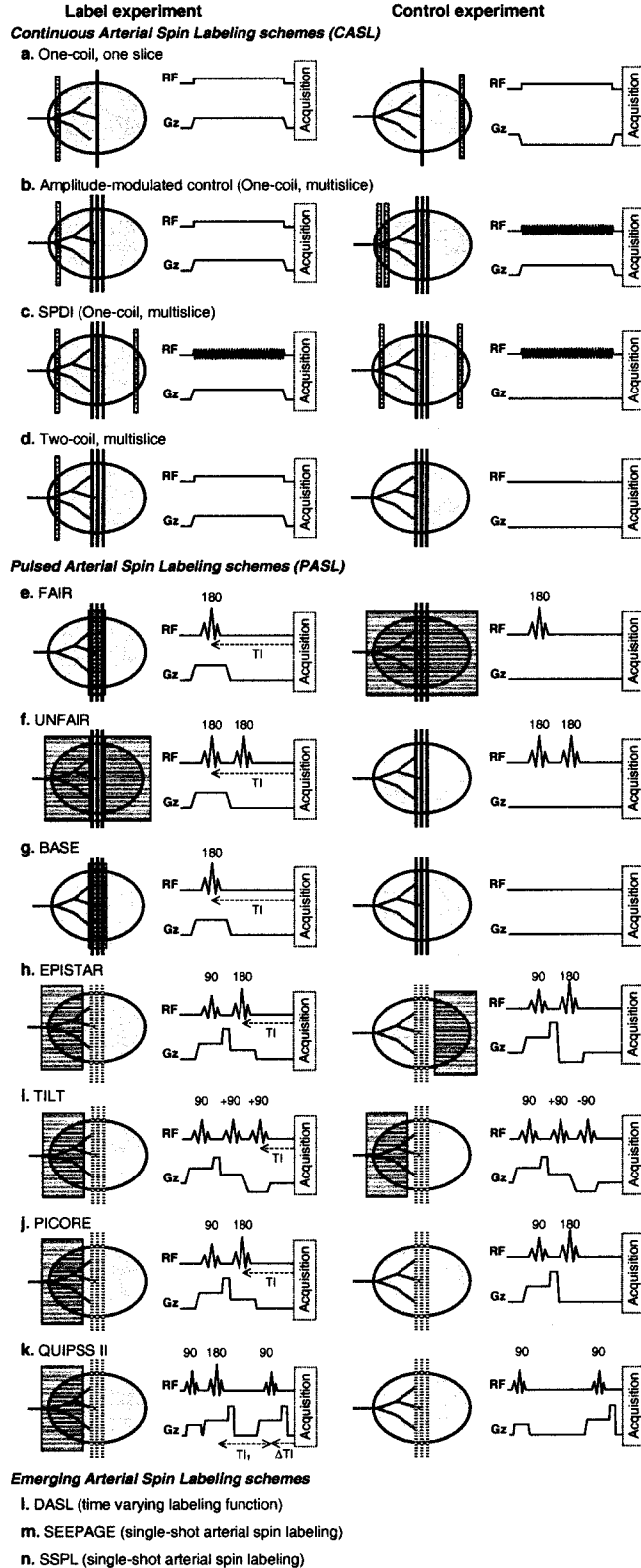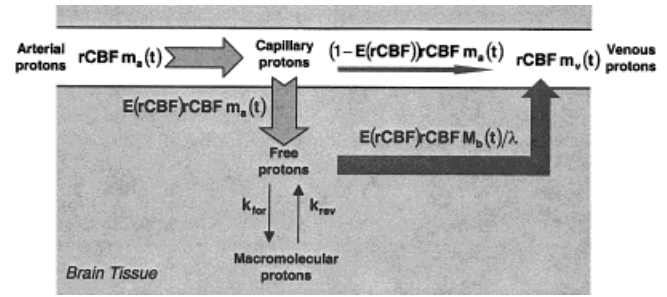

Figure 6. Schematic of the different exchange processes that occur within a voxel. A blood flow- dependent fraction, E(rCBF), of labeled water crosses the BBB, while the remaining arterial water flows to veins. In reverse, tissue water passes the BBB and reaches the venous compartment. Within the extravascular compartment, there is a permanent exchange between free water molecules and macromolecular water molecules. (After Silva et al (166))

imaging plane, saturates the magnetization of macromolecular protons within the slice of interest. Assuming $M_m(t) = 0$, Eq. [39] becomes

$$\frac{dM_t(t)}{dt} = \frac{M_t^0 - M_t(t)}{T_{1t,\text{sat}}} + \text{rCBF } E[m_a(t) - m_v(t)], \quad (41)$$

where

$$T_{1t,\text{sat}} = \left(\frac{1}{T_{1t}} + k_{\text{for}}\right)^{-1}. \qquad (42)$$

Since the macromolecular magnetization is saturated, the free proton magnetization is decreased due to cross-relaxation between water molecules and adjacent macromolecules (29,31,161). In order to properly account for the effect of off-resonance saturation on the tissue water magnetization, one needs to acquire a control signal from the tissue with the same off-resonance

Figure 5

Figure 5. Diagrams of different ASL schemes. For all schemes (**a-k**), the experiment yielding label images and the experiment yielding control images are briefly summarized. Each experiment is described by two diagrams: the first one represents the respective positions of the labeling planes and the imaging slices on tissue (egg-shaped object) and feeding arteries; the second shows a summary of the MR sequence (RF pulse and slice gradient waveform). The timing of the sequence is not to scale. ▢ represents an inversion area, ▬ represents the slices, and ······ represents the slices after a saturation pulse has been applied. Gz, slice selection gradient; TI, inversion time. All flip angles are given in degrees. SPDI, simultaneous proximal and distal irradiation; EPISTAR, echo-planar imaging and signal targeting with alternative radiofrequency; FAIR, flow-sensitive alternating inversion recovery; UNFAIR, un-inverted flow-sensitive alternating inversion recovery; BASE, unprepared basis and selective inversion; TILT, transfer insensitive labeling technique; PICORE, proximal inversion with control for off-resonance effects; QUIPSS, quantitative imaging of perfusion using a single subtraction; DASL, dynamic arterial spin labeling; SEEPAGE, spin-echo entrapped perfusion image; SSPL, single-shot perfusion labeling technique.
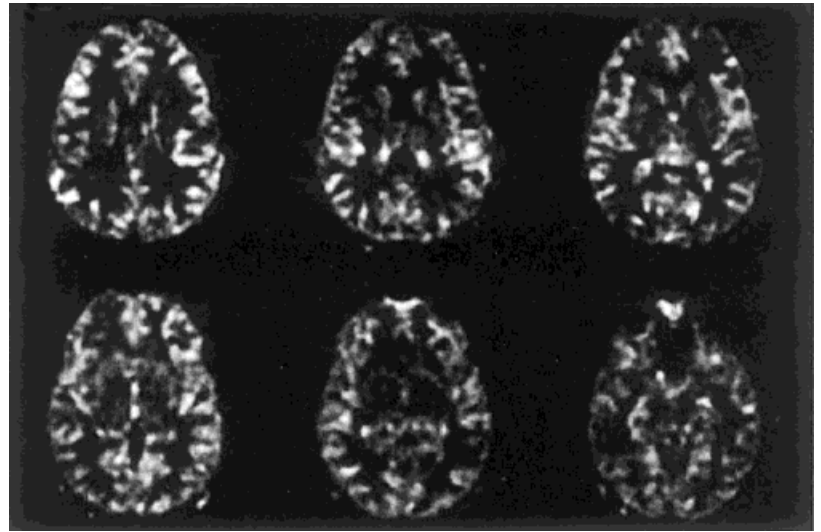
Figure 7. Example of CBF maps obtained in the human brain with an ASL technique. These maps were obtained at 1.5 T by S. Lalith Talagala, using SPDI CASL (unpublished data). RF at two frequencies was obtained by cosine amplitude modulation at 15.625 KHz. The labeling plane was positioned $\approx$115 mm from the center of the imaged region and each experiment (label and control) was averaged 50 times. Maps are 1 cm thick, and the in-plane resolution is $\approx$3.1 mm. (Courtesy of S. Lalith Talagala)

saturation but without labeling. This can be achieved by applying an RF pulse at a frequency symmetrical to the labeling frequency with respect to the imaging plane frequency (29,31,161). Using flow-driven adiabatic inversion, Zhang et al showed that rCBF could be quantified with (31,161)

$$\text{rCBF} = \frac{\lambda}{ET_{1t}} \left(\frac{M_t^{\text{con}}(TR) - M_t^{\text{lab}}(TR)}{(2\alpha(\tau) - 1)M_t^{\text{con}}(TR) + M_t^{\text{lab}}(TR)} \right), \quad (43)$$

where $M_t^{\text{con}}(TR)$ and $M_t^{\text{lab}}(TR)$ are the tissue magnetizations at the TR time in control state (i.e., when arterial spins have not been inverted) and in label state (i.e., when arterial spins have been inverted).

In order to apply this method in humans, the labeling and the control pulses need to be split in trains of pulses to reduce the RF power deposition. For example, at 1.5 T, Roberts et al used a train of 74-msec RF pulses at about 26 mG, followed by a 26-msec delay (so that the duty cycle is 74%) to obtain a pseudo continuous inversion during 2.4 seconds (167).

Multislice Schemes With One-Coil CASL

The scheme proposed by Detre et al only allows quantification of blood flow in a single slice, as the control and the label RF irradiations are only compensated at a single slice (29,168). In order to quantify rCBF in multiple slices with a single coil, Alsop et al first proposed to invert the already inverted arterial spins by applying an amplitude-modulated RF irradiation (a constant RF irradiation multiplied by a sine wave) during the acquisition of the control signal (Fig. 5b) (168). In the control case, arterial spins are inverted twice after flowing through the two inversion planes. Because both label and control pulses are applied at the same center frequency and with the same averaged power, their saturation effects on the macromolecular magnetization in the remote brain tissue are nearly identical (168). The major limitations of this setup are the RF power deposition and the fact that the double inversion is not perfect; the labeling efficiency is therefore reduced.

Talagala et al also developed the simultaneous proximal and distal irradiation (SPDI) method, in which equal RF power is applied proximally and distally to the slices to be imaged (169). The application of RF simultaneously at two different frequencies generates a saturation profile, which is symmetric and reasonably flat around the midpoint frequency. Label images are obtained in the presence of a magnetic field gradient and control images are obtained in the absence of gradient (Figs. 5c and 7). The major limitations of this setup are the RF power deposition and the fact the flat profile does not extend over a large region of tissue, thereby limiting the number of slices that can be acquired.

Two-Coil CASL

Using two different coils, it is possible to prevent the tissue from being irradiated during the application of the labeling pulse, as shown by Silva et al and Zhang et al (165,170) (Fig. 5d). The two-coil system consists of a small labeling coil placed near the carotid arteries and a second coil, which is actively decoupled from the labeling coil, to image the tissue. Because of the coupling between tissue and macromolecular magnetization, the quantification of blood flow is different from the one-coil case. rCBF can be determined using (170):

$$\text{rCBF} = \lambda \left(\frac{1}{T_{1t}} + \delta \right) \frac{M_t^0 - M_t^{\text{lab}}}{M_t^{\text{lab}} + (2\alpha - 1)M_t^0}, \quad (44)$$

where

$$\delta = \frac{k_{\text{for}}}{1 + k_{\text{rev}}T_{1m}}. \quad (45)$$

δ only depends on the magnetization transfer rate (k_{for}, k_{rev}) and on the spin-lattice relaxation time constant of the macromolecular spins, T_{1m}. According to Zhang et al, ignoring δ in the quantification of rCBF would cause an approximately 17% underestimation of blood flow in the rat brain at 4.7 T (165).

Using a two-coil system reduces the RF power deposition, which can be critical for human studies (171). Using separate label and imaging coils also allows the labeling of an artery and the mapping of the perfused territory of this particular artery (170,171).

Two-Coil vs. One-Coil CASL

In terms of SNR per unit of acquisition time, the use of a two-coil system is not always advantageous. In the one-coil situation, the saturation of the tissue macromolecule magnetization induces both a reduction in the free proton magnetization and in the apparent tissue spin-lattice relaxation time (from T_{1t} to $T_{1t,sat}$). In some cases, the T_{1t} reduction may allow sufficient averaging to compensate for the reduction in free protons magnetization, within the same acquisition duration as that for the two-coil setup. Moreover, the labeling coil has to be placed near a carotid artery. The label is therefore performed further upstream from the tissue than with a one-coil setup, leading to a reduced degree of labeling at the imaging site. However, the two-coil system allows for multiple slices to be acquired without any magnetization exchange problem and, for a true continuous labeling, with little RF deposition limitation. Usually, it is also the setup that maintains the tissue T_{1t} and the blood T_{1a} as similar as possible, which is important for CBF quantification (cf. section 5, "Quantification of Blood Flow Using ASL Techniques"). A strategy to optimize the SNR using one-coil CASL has been proposed by Lei and Peeling (172), in which they considered a partial saturation of the macromolecular magnetization.

Methodological Improvements

Several methodological improvements have been proposed to improve CASL methods. Zhang et al proposed an alternated-line-scanning method to further combine the acquisition of the control and the label images, taking advantage of the small differences between the two images (173). Pekar et al observed an apparent asymmetry—around the chemical shift of the water signal—in the effects of off-resonance RF irradiation on the intensity of the MR signal from water protons (174). They proposed a four-step acquisition protocol to correct for any possible asymmetry in the magnetization transfer spectrum (174).

The contribution of labeled water in large vessels was not included in the original physiological model, as the crusher gradients applied suppressed the contribution of fast-moving spins (29,161). Since the first experiments were carried out at 4.7 T on small animals, this contribution was not a significant problem (i.e., the in-plane resolution was ~300 μm and therefore the largest vessels would have been arterioles). However, in humans, Ye et al pointed out that the arterial bed contributes to about 50% of the total blood flow signal. They also recommended the use of crusher gradients to defocus fast-moving spins (175). Ye et al also showed that suppressing the contribution of fast-moving spins also had an effect on the apparent transit time of the labeled blood. It is, however, impossible to clearly dif-

ferentiate fast-moving spins from slow-moving spins with bipolar gradients, as shown by Le Bihan et al and Henkelman et al in their intravoxel incoherent motion studies (176,177).

The transit time from the labeling plane to the imaging plane is not uniform across a slice or between slices (161,178). Alsop and Detre reduced the sensitivity of the CASL techniques to transit time heterogeneity by inserting a postlabeling delay between the labeling pulse and the acquisition module in order to let slow-moving spins reach the tissue (179).

Pulsed ASL (PASL)

Main Methods

Instead of labeling blood as it flows through a plane, PASL techniques rely on the labeling of a large blood volume with a short RF pulse. To obtain thick inversion slabs with sharp edges, adiabatic pulses are generally used. The volume of labeled blood then flows into the tissue during the time TI. In 1992, Kwong et al first used an inversion-recovery sequence to obtain CBF-weighted images of the brain during visual stimulations (151). This idea was further developed by Kwong et al (180), Schwarzbauer et al (181), and Kim (178), who named the approach flow-sensitive alternating inversion recovery (FAIR) (Fig. 5e). In FAIR, the label image is acquired after a slice-selective inversion and the control after a nonselective inversion (Fig. 5e). In order to maintain the integrity of the image slice, the inversion slab (with its imperfect edges) has to be applied at some distance from the volume that will be imaged. Kim recommended using a ratio of at least 3:1 between the thickness of the image slab and the thickness of the inverted volume (178). Multiple slices can also be contained in the inversion slab. However, the different slices will experience different transit times, which makes quantification difficult. Sequences derived from FAIR are as follows:

- Uninverted FAIR (UNFAIR), by Helpern et al, in which the stationary spins within the imaging slice stay uninverted (182). With this technique, the control image is entirely flow independent, so it needs to be acquired only once (Fig. 5f).
- BASE, by Schwarzbauer and Heinke (183), consists of unprepared basis (BA) images, which serve as a control, and selective (SE) inversion prepared images, which are sensitive to blood flow (Fig. 5g). Since the BASE scheme does not require a nonselective inversion, it can be used with small coils.
- FAIR with an extra RF pulse (FAIRER), by Mai and Berr (184), in which an extra slice-selective saturation pulse is added. With this scheme, the order in which control and label images are subtracted does not depend on the TI value, which is not the case with FAIR.
- Zhou et al also used the acronym FAIRER, but to designate FAIR excluding radiation damping (185). In this method, weak magnetic field gradients are applied during the inversion recovery and spin-echo delays to limit the effect of the radiation damping of the RF pulses on the flow measurement.

In 1994, Edelman et al proposed the echo-planar imaging and signal targeting with alternating radio frequency (EPISTAR) technique that combined a spin-labeling RF pulse with an echo-planar acquisition (Fig. 5h) (186). In EPISTAR, the label image is acquired after saturation of the tissue signal and inversion of the inflowing spins. The control image is acquired in the same conditions, but the inversion pulse is applied equidistant above the imaged slices. Like FAIR, EPISTAR was also adapted in various ways:

- Chen et al replaced the echo-planar imaging sequence by a single-shot turbo spin echo, to reduce the sensitivity of the imaging technique to susceptibility effects, and called their method STAR-HASTE (187).
- Edelman et al more recently proposed an improvement of their method, in which they replaced the inversion pulse in the label experiment by an adiabatic 360° RF pulse and the control inversion pulse by two 180° RF pulses (188). The adiabatic 360° RF pulse inverts the spins (label), but the two 180° pulses counteract each other and leave the spins uninverted (control). As the same RF power is applied during the label and the control experiments, the magnetization transfer effects are identical.
- Based on EPISTAR, Golay et al proposed a method insensitive to magnetization transfer effects, called transfer insensitive labeling technique (TILT) (189) (Fig. 5i). In this method, the inversion pulse was replaced by two consecutive 90° RF pulses for the label image and by two 90° RF pulses with opposite phases (so that they have no net effect) for the control.
- Wong et al modified EPISTAR to reduce the effect of slice profile imperfection and to improve the sensitivity to inflow (190). In proximal inversion with control for off-resonance effects (PICORE), Wong et al replaced the inversion slab in the control acquisition by an RF pulse applied at the same frequency as in the label experiment but in the absence of a magnetic field gradient (Fig. 5j).

To reduce the sensitivity of techniques like EPISTAR or FAIR to transit time, Wong et al introduced two schemes, quantitative imaging of perfusion using a single subtraction (QUIPSS) and QUIPSS II (191). In QUIPSS, a saturation pulse is applied to the imaging planes after the application of the labeling RF pulse. Because the saturation pulse is applied for both the label and the control images, the contribution to the signal from blood that was in the imaging slices prior to the saturation pulse disappears when computing the difference between label and control images. In QUIPSS II, the saturation pulse is applied after the labeling pulse on the same slice that was labeled (Fig. 5k). This produces a well-defined bolus of labeled blood, which facilitates the CBF quantification (191,192). Luh et al replaced the saturation pulse in the QUIPSS II scheme by a train of thin-slice saturation pulses, applied periodically (192). Since thin-slice sinc pulses have a better B_1 homogeneity over the slice and sharper edges than a thick-slice pulse, the new method (called Q2TIPS for QUIPSS II with thin-slice TI periodic saturation) allows for better quantification of rCBF.

Quantification

With PASL techniques, the method for quantification of CBF is different from the one used with CASL techniques, although it relies on the same theoretical background as presented by Detre et al (29) (cf. section 5, Basic Principles of ASL). The first model for PASL was proposed by Kim and Kwong et al (178,180). They showed that the difference between control and label tissue magnetization could be computed with:

$$\Delta M_t = 2M_t^0 \, TI \, \frac{rCBF}{\lambda} \exp(-TI/T_{1t}). \tag{46}$$

Calamante et al proposed a more complete approach, accounting for differences between blood and tissue T_1 and for labeling efficiency (193):

$$\Delta M_t = 2\alpha_0 M_t^0 \frac{rCBF}{\lambda} \left[\frac{\exp(-TI/T_{1t,\text{app}}) - \exp(-TI/T_{1a})}{1/T_{1a} - 1/T_{1t,\text{app}}} \right]. \tag{47}$$

Buxton et al recently proposed a general model for quantification of CBF using PASL techniques (154). Their model takes into account the QUIPSS II approach, in which the duration of the bolus of labeled spins is well defined, and also accounts for the finite transit time of labeld spins.

Methodological Improvements

The use of crusher gradients to reduce the contribution of labeled spins located in large vessels has also been adopted in PASL techniques (190). However, the signal from large arteries can be sufficiently destroyed during the time course of an echo-planar acquisition without the need of additional bipolar gradients (154).

When multiple slices are acquired at different TIs, they have different CBF weighting, due to differences in blood transit time. Kao et al implemented FAIR with the Hadamard encoding technique (simultaneous multi-slice acquisition with arterial-flow tagging (SMART)) in order to simultaneously acquire multiple slices (194). Yang et al implemented FAIR with a spiral imaging, taking advantage of its short acquisition duration (22 msec) to acquire up to 10 slices per labeling period (195).

To perform inversion of thick slabs in PASL techniques, hyperbolic secant pulses have mostly been used. It is, however, desirable to obtain inversion profiles that closely match the imaging profiles, so that inversion slabs and imaging slabs can be superimposed or juxtaposed (Fig. 5e–k). In most of the PASL techniques, a saturation pulse is applied on the imaging slices because it helps to minimize the effect of imperfect slice profiles (186,191). In order to improve the inversion profile, Yongbi et al adapted a C-shaped frequency corrected inversion ((FOCI) Ordidge et al (196)) pulse for the ASL experiment (181). The use of FOCI

pulses is particularly interesting at low fields (like 1.5 T), where the tissue T_{1t} is short.

To increase the sensitivity of ASL, Ye et al recently proposed to use inversion pulses to reduce the contribution of static tissue spins to the signal (197), as previously suggested by Dixon et al for angiography (198). This technique, in which noise reduction is achieved by attenuating the static signal in arterial spin tagging (ASSIST), is a modification of the FAIR approach. Two nonselective inversion pulses are applied during the preparation phase to minimize the contribution of static protons.

Emerging ASL Schemes

Dynamic ASL

In order to simultaneously determine rCBF, transit time, and T_{1t}, Barbier et al measured the response of the tissue magnetization to a label that varied with time, the labeling function (199). With dynamic ASL (DASL), there is no subtraction between a control and a label image. The tissue response to the labeling function (e.g., a square function) is fitted by the equation predicting the tissue response (Fig. 8). From the fit, the blood transit time to the perfusion site, the tissue T_{1t}, and the tissue blood flow can be simultaneously extracted, yielding a more accurate quantification of CBF without the need of a postlabeling delay. Moreover, as the transit time can be mapped for each separate slice, the quantification of rCBF in each slice is not affected by its position. The use of a periodic labeling function makes the tissue response periodical, allowing for the filtering out of periodical noise perturbations. DASL also has the potential to distinguish the vascular contribution from the CBF, based on the shape of tissue response (200).

Single-Shot ASL

New ASL techniques are appearing to directly acquire an rCBF map, avoiding the acquisitions of a control and a label map. Based on an idea by Dixon et al, who suggested that multiple inversion pulses could be used to reduce the static tissue signal in order to better measure the flowing blood contribution (198), Blamire and Styles proposed a new method, called spin-echo entrapped perfusion image (SEEPAGE) (201). After saturating the signal from the slices of interest, a train of inversion pulses is applied to prevent the static tissue signal from recovering. Unsaturated flowing spins can then be detected, their contribution to the signal being above the static tissue signal. Recently, Duyn et al proposed a single-shot perfusion labeling technique (SSPL). The technique is similar to the approach of Kwong et al (151), but two inversion pulses have been added to null the static tissue magnetization so that the magnetization of flowing spins can be readily detected (202), as proposed in the ASSIST method (197).

Quantification of Blood Flow Using ASL Techniques

Problematic Issues

The amount of blood water extracted by the tissue is still not well known. Originally, Detre et al assumed
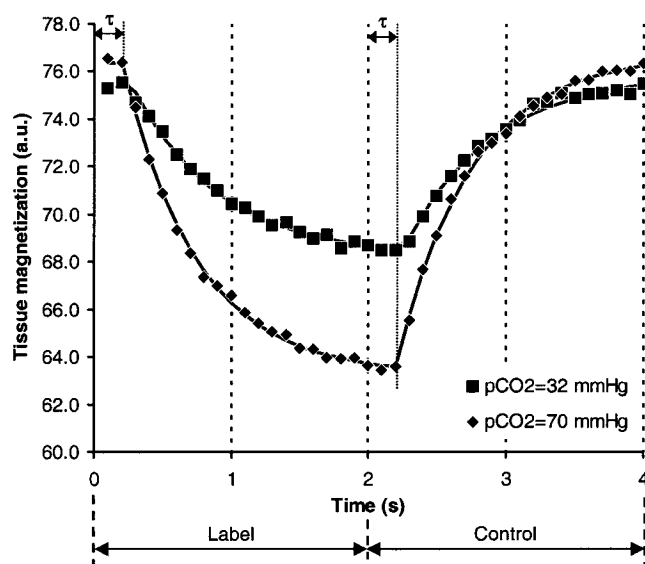

Figure 8. Time courses of the responses of a voxel in a rat brain, at two different arterial pCO_2, to a square labeling function. Data were acquired at 4.7 T using the interlaced DASL scheme (199), with a temporal resolution of 100 msec. The voxel size was $0.4 \times 0.4 \times 2$ mm^3. Squares and diamonds represent raw data, and continuous lines represent the best fits, using a physiological model based on Eq. [41] predicting the theoretical tissue response. τ stands for transit time from the labeling plane to the perfusion site. Below the time scale, the two half-periods of the square labeling function are indicated: "label" when the labeling pulse is applied at the labeling frequency and "control" when the labeling pulse is applied at the control frequency. The voxel magnetization decreases as labeled spins enter the voxel and increases as unlabeled water enters the voxel. The response of the tissue magnetization is shifted in time with respect to the input function due to the transit time. (Data from Emmanuel Barbier)

that the labeled water is completely extracted into tissue. However, Silva et al demonstrated, using ASL, that only about 80% of water is extracted into brain tissue in a rat under normocapnic condition (166,203) (Fig. 9). However, low water extraction fractions may not necessarily yield a blood flow underestimation. Indeed, in a recent approach toward a general kinetic model for ASL, Buxton et al pointed out that complete extraction could be assumed because of the finite transit time of water through the voxel (154). More recently, St. Lawrence et al studied the effect of restricted water exchange on rCBF calculated from ASL measurements (204). Their mathematical approach showed that, in humans, the capillary contribution to the MR signal may play a significant role in ASL experiments and, in fact, counterbalances the effect of restricted water exchange between blood and tissue (Fig. 10). Their results are in good agreement with Buxton et al. Therefore, even in the presence of exchange limitations, the measured CBF should be in good agreement with true CBF, provided that blood and tissue T_1s are similar and that no labeled blood leaves the voxel through the venous system. Ewing and Fenstermache obtained similar results for the CASL case in rats (205). The fact that the capillary compartment significantly contributes to the
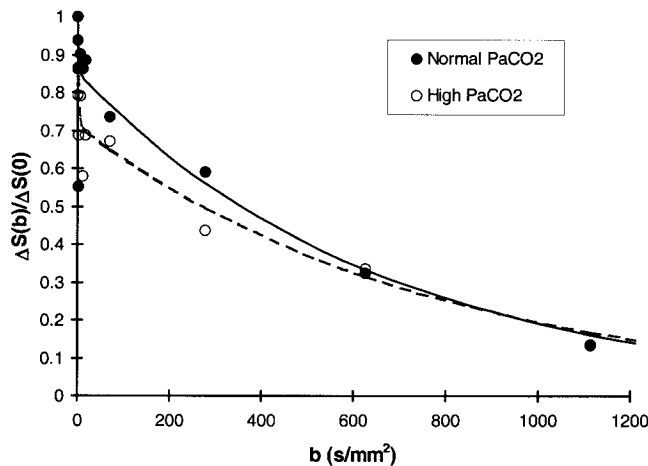
Figure 9. Attenuation curves of difference signal for a rat under normocapnic conditions (arterial pCO_2 = 22 mm of Hg, filled circles) and hypercapnic conditions (arterial pCO_2 = 78 mm of Hg, open circles). The curves were obtained by subtracting the label signal from the control signal at each b value. The lines represent the best nonlinear least-squares fit to the data using $\Delta S(b)/\Delta S(0) = (1 - E)\exp(-bD^*) + E\exp(-bD)$, where E is the water extraction fraction, and D^* and D are the slow and the fast apparent diffusion coefficients (ADC), respectively; D^* is associated to the labeled water in the tissue and D is associated to the labeled water in the vasculature. For this animal, E was 0.85 ± 0.08 at low arterial pCO_2 and 0.71 ± 0.06 at high arterial pCO_2; D^* was (1.50 ± 0.47) 10^{-3} $mm^2 \cdot second^{-1}$ at low arterial pCO_2 and (1.30 ± 0.35) 10^{-3} $mm^2 \cdot second^{-1}$ at low arterial pCO_2; D was (407 ± 869) 10^{-3} $mm^2 \cdot second^{-1}$ at low arterial pCO_2 and (407 ± 405) 10^{-3} $mm^2 \cdot second^{-1}$ at high arterial pCO_2. (Courtesy of Afonso C. Silva. For other data, see reference 203)

signal does not imply that crusher gradients should not be used, since labeled spins within small vessels are not affected by the typical crusher gradient strength used in ASL experiments (175,203). Note that the permeability to water of the BBB is different between species (42,43,206,207) and could also be different between pathological and normal tissues (43).

Nevertheless, for high flow values (more specifically in animal models), it can occur that labeled spins leave the voxel through the venous system. This depends on the amount of water extracted by tissue and on the ratio between T_{1a} (the blood T_1) and the transit time through the voxel. If the transit time through the voxel is short enough, compared to T_{1a}, unextracted water molecules will exit the voxel while still labeled. This has been observed in large veins of the rat brain by Barbier et al (200). Based on the previously mentioned works of Buxton et al and St. Lawrence et al, this phenomenon leads to an underestimation of rCBF, unless the extraction fraction can be measured. Buxton et al also mentioned that labeled venous blood (either by the label or by the control pulse), which subsequently moves into the voxel, could lead to an error on rCBF quantification (154).

The tissue $T_{1t,app}$, which is an important parameter for CBF quantification, has been observed to be spatially heterogeneous early after controlled cortical impact (30% difference between contusion and normal

tissue) by Hendrich et al (208). This study points out the importance of measuring $T_{1t,app}$ for rCBF quantification purposes, especially in pathological cases. Moreover, when a voxel contains gray matter and cerebrospinal fluid, its average $T_{1t,app}$ may be overestimated, leading to an underestimation of rCBF. Also, when cerebrospinal fluid is present in the voxel, the mass of tissue present in that voxel is overestimated and the true flow per gram of tissue is therefore underestimated (154,180). The blood T_1 depends on the cellular content of the blood and therefore on the Hct. Differences between blood T_1 and tissue T_1 also lead to errors in the ASL quantification (193,204,205). At 1.5 T in the human brain, this implies that the CBF quantification will be more accurate in the gray matter than in the white matter, as the gray matter and blood T_1s are closer than white matter and blood T_1s (193).

The heterogeneity of the blood-brain partition coefficient for water, λ, may also affect CBF quantification.

a. PS=140 ml/100g/min
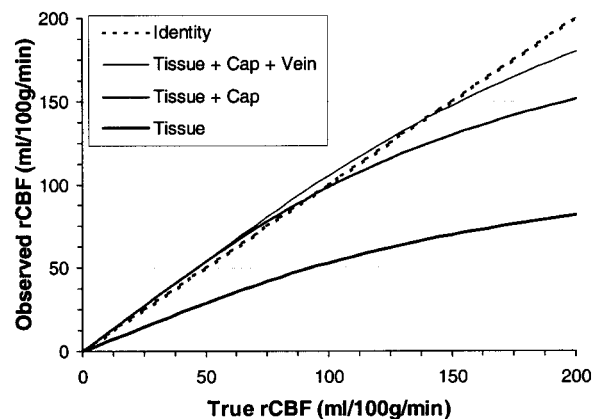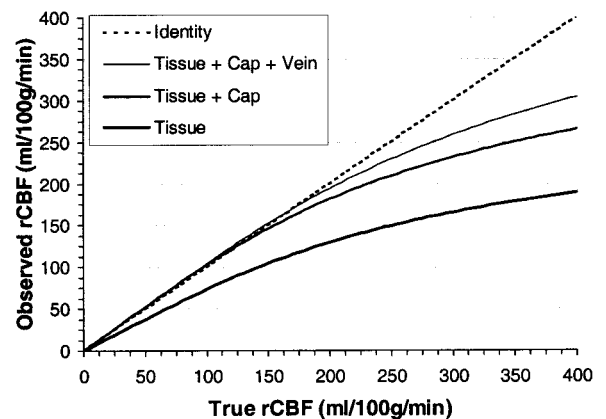

b. PS=300 ml/100g/min

Figure 10. Numerical simulations of observed values of CBF as a function of true CBF, based on the single-pass approximation model (204). The permeability surface area products are 140 mL/100 g/minute (**a**), which corresponds to human brain, and 300 mL/100 g/minute (**b**), which corresponds to the rat brain. For these simulations, the blood T_{1a} is 1.2 seconds, the tissue T_{1t} is 1.0 seconds, and the capillary and venous blood volumes are 2% each. The arterial contribution to the signal is not accounted for in this model, since it can be removed using crusher gradients, (Courtesy of Keith St. Lawrence. For other simulations, see reference 204)

The variation of water content between gray and white matters affects λ (155,156). In brain lesions, λ could be very different from its normal value (208). Roberts et al proposed a method to map this coefficient using proton density MR images (156).

The BOLD contrast mechanism, discovered by Ogawa et al (209), also needs to be accounted for in ASL studies, either for normal or for activation studies. Since the tissue T_2^* (and T_2) depends on the blood oxygenation level (209), and therefore on the blood location within the vasculature (i.e., arteries, capillaries, or veins), the contributions of the various components of the vasculature to the MR signal are different. In activation studies using ASL, simultaneous changes in blood oxygenation and in rCBF yield complex signal variations. Baseline measurements are then required to separate oxygenation from perfusion changes when comparing control and label images (178). The use of short echo time imaging techniques, like spiral imaging, reduces the effects of the blood oxygenation (temporal or spatial).

Validation by Other Methods

Despite the above-mentioned issues regarding quantification of ASL measurements, the results from validation studies are encouraging. Walsh et al (210) compared rCBF measurements obtained in rats with ASL and with microspheres. They obtained a mean error of $-32.4 \pm 20.2\%$ and showed that ASL could underestimate rCBF at high flow rates. Pell et al compared ASL and hydrogen clearance measurements in the gerbil at 2.35 T. They found a good agreement between both methods for low flow rates, but at flow rates above 80 mL/100 g/minute, ASL yields higher CBF values than hydrogen clearance (211). Ewing et al compared CASL and ^{14}C-iodoantipyrine autoradiography measurements in rats and obtained a strong relationship between the measurements from the two techniques (212). The differences between the two techniques are due in part to the difference in slice thickness: 2 mm with MR and 20 μm with autoradiography. Hoehn et al also compared these two techniques in rats with about the same slice thickness as Ewing et al and found an average linear correlation coefficient of 0.86 (213). However, ASL-based measurements were offset with respect to the autoradiography data. The offset was most certainly due to the differences in slice thickness. More recently, Ye et al compared rCBF measurements in the human brain obtained with PET and ASL by registering the low resolution $H_2^{15}O$ data with the high-resolution MR data (214). In gray matter, no statistical difference was found between the two techniques. In white matter, ASL yielded an underestimation of rCBF ($\sim$20%), which the authors attributed to an underestimation of the arterial transit time in white matter. Quantitative blood flow values obtained by ASL can also be compared to quantitative blood flow values from the literature, provided that the experimental conditions are similar (215).

Applications of ASL Techniques

ASL techniques have already been used in numerous applications, as recently reviewed by Calamante et al (153) and Detre and Alsop (216).

In functional studies, ASL has been used in rats (217) and in humans (151,218–220). Results of ASL-based and BOLD-based functional MRI experiments have also been compared. Some ASL techniques have been adapted to simultaneously measure changes in blood flow and in BOLD contrast, using a first CBF-weighted echo and a second BOLD-weighted echo. Activation maps based on BOLD and on CBF acquisitions were compared both in humans and animals (221–223). Recently, Gonzalez-At et al used ASL to measure the functional changes in the transit time from the labeling plane to the imaging plane (224), an effect previously observed by Belle et al using a functional angiography technique (225).

As ASL measurements can be repeated over time easily and with total noninvasiveness, they are well suited for longitudinal studies. ASL techniques have been applied in pharmacological studies, like in the follow-up of the systemical delivery of amphetamines or of local delivery of picrotoxinin to the brain (170,226). The brain reactivity to CO_2 (227) and the influences on CBF of various anesthetics have also been characterized using ASL (228).

Blood pool agent approaches and ASL can also be performed successively (229) or combined (118) to obtain CBV and CBF maps.

Finally, ASL has also proven its usefulness in the study of various pathologies, in animals or in humans:

- Animal models of transient occlusion of the middle cerebral artery (230–234);
- Strokes (235–237);
- Traumatic brain injuries (208,227);
- Degenerative brain diseases (238);
- Brain tumors (239–241).

Perfusion quantification is complicated in brain lesions, since it is not clear what become the correct values of (1) T_{1t}, (2) the blood-brain partition coefficient for water, (3) the BBB permeability, and (4) the transit time to the lesion, which might be longer (208,241). As the transit time to the lesion increases, the ability of accurately measuring CBF decreases.

CONCLUSION

The last 15 years have seen a tremendous development of MR methods for brain perfusion imaging, and numerous studies have now shown that MRI measurements of rCBV and rCBF are possible. Both functional and clinical MRI have already benefited from the new techniques. Current applications include the evaluation of the vasodilatory capacity of the brain during cerebral perturbations, the study of disease processes that alter the microvasculature, and attempts to the early prediction of the histological outcome in stroke.

Originally, the models developed to analyze measurements obtained in experiments based either on nondiffusible or on diffusible tracers were rather different. In

both approaches, however, it appears that an accurate characterization of brain perfusion asks for some refinement and that, for instance, arteriolar, capillary, and venous contributions to the signal should be distinguished. These refinements tend to make the models more homogeneous, although some interesting differences remain, like in the way water exchange between blood and tissue has to be accounted for.

Contrast-enhanced bolus tracking techniques are well suited to obtain fast, low-resolution information on brain perfusion. Contrast-enhanced steady-state techniques using exogenous agents have the ability to provide higher spatial resolution and quantitative measurements of rCBV, but at the expense of longer acquisitions. With ASL methods, quantification of rCBF requires more time, compared to the acquisition of a relative rCBF map, since the tissue T_1 and possibly the transit time have to be measured. Depending on the type of information desired, a large variety of tools is thus available, from a low spatial resolution map of relative values to a quantitative, high spatial resolution map of CBV or CBF. As always, the quality of the information depends on the time available for acquisition.

However, even if the results obtained so far are extremely promising, it should be stressed that perfusion MRI is still in an early stage of its development. Further work is necessary to address the numerous quantification problems, to bring the robustness required in a clinical environment, and to further validate in the context of various pathologies the methods that have been assessed on normal tissues. Finally, it might be expected that MR technology improvements in years to come will give access to higher spatial resolution and current MRI methods and models to measure brain perfusion will need further adaptations, as the voxel size will approach the arteriolar scale.

ACKNOWLEDGMENTS

REFERENCES

1. Bloembergen N, Purcell EM, Pound RV. Relaxation effects in nuclear magnetic resonance absorption. Phys Rev 1948;73:679–712.
2. Hahn EL. Spin echoes. Phys Rev 1950;80:580–594.
3. Suryan JR. Nuclear resonance in flowing liquids. Proc Indian Acad Sci 1951;A33:107–111.
4. Stilbs P. Fourier transform pulsed gradient spin-echo studies of molecular diffusion. Prog Nucl Magn Reson Spectrosc 1987;19:1–45.
5. Callaghan PT. Principles of nuclear magnetic resonance microscopy. Oxford: Clarendon Press, 1991.
6. Fukushima E, Roeder SW. Experimental pulse NMR: a nuts and bolts approach. Reading: Addison-Wesley; 1981.
7. Le Bihan D. Diffusion NMR imaging. Mag Reson Quarterly 1991; 7:1–30.
8. Sanders JA, Orrisson Jr WW. Functional magnetic resonance imaging. In: Orrisson Jr WW, Lewine JD, Sanders JA, Hartshorne MF, editors. Functional brain imaging. St. Louis: Mosby-Year Book, Inc.; 1995. p 239–326.
9. Caprihan A, Fukushima E. Flow measurements by NMR. Phys Rep 1990;4:195–235.
10. van As H, Schaafsma TJ. Flow in nuclear magnetic resonance imaging. In: Petersen SB, Muller RN, Rinck PA, editors. An introduction to biomedical resonance. Stuttgart, New York: Verlag; 1985. p 68–96.
11. Le Bihan D. Diffusion and perfusion magnetic resonance imaging. Applications to functional MRI. New York: Raven Press; 1995. 374 p.
12. Rosen BR, Belliveau JW, Chen D. Perfusion imaging by nuclear magnetic resonance. Mag Reson Quarterly 1989;5:263–281.
13. Rosen BR, Belliveau JW, Vevea JM, Brady TJ. Perfusion imaging with NMR contrast agents. Magn Reson Med 1990;14:249–265.
14. Rosen BR, Belliveau JW, Aronen HJ, et al. Susceptibility contrast imaging of cerebral blood volume: human experience. Magn Reson Med 1991;22:293–299.
15. Le Bihan D. Theoretical principles of perfusion imaging. Application to magnetic resonance imaging. Invest Radiol 1992;27(Suppl 2):6–11.
16. Le Bihan D, Douek P, Argyropoulou M, Turner R, Patronas N, Fulham M. Diffusion and perfusion magnetic resonance imaging in brain tumors. Top Magn Reson Imaging 1993;5:25–31.
17. Renshaw PF, Levin JM, Kaufman MJ, Ross MH, Lewis RF, Harris GJ. Dynamic susceptibility contrast magnetic resonance imaging in neuropsychiatry: present utility and future promise. Eur Radiol 1997;7(Suppl 5):216–221.
18. Bandettini PA, Wong EC. Magnetic resonance imaging of human brain function. Principles, practicalities, and possibilities. Neurosurg Clin N Am 1997;8:345–371.
19. Sorensen AG, Tievsky AL, Østergaard L, Weisskoff RM, Rosen BR. Contrast agents in functional MR imaging. J Magn Reson Imaging 1997;7:47–55.
20. Bovee WM, Rozijn TH, Van Der Sanden BP, Heerschap A. NMR perfusion and metabolic imaging and some examples on brain tumours. Cell Mol Biol (Noisy-le-grand) 1997;43:675–689.
21. Lev MH, Hochberg F. Perfusion magnetic resonance imaging to assess brain tumor responses to new therapies. Cancer Control 1998;5:115–123.
22. Neumann-Haefelin T, Moseley ME, Albers GW. New magnetic resonance imaging methods for cerebrovascular disease: emerging clinical applications. Ann Neurol 2000;47:559–570.
23. Duyn JH, van Gelderen P, Frank JA, Mattay VS, Moonen CTW. 3D bolus tracking with frequency-shifted BURST MRI. J Comput Assist Tomogr 1994;18:680–687.
24. van Zijl PC, Eleff SM, Ulatowski JA, et al. Quantitative assessment of blood flow, blood volume and blood oxygenation effects in functional magnetic resonance imaging. Nat Med 1998;4:159–167.
25. Walovitch RC, Williams SJ, Lafrance ND. Radiolabeled agents for SPECT imaging of brain perfusion. Int J Rad Appl Instrum B 1990;17:77–83.
26. Todd MM, Weeks JB, Warner DS. The influence of intravascular volume expansion on cerebral blood flow and blood volume in normal rats. Anesthesiology 1993;78:945–953.
27. Bereckzi D, Wei L, Otsuka T, et al. Hypoxia increases velocity of blood flow through parenchymal microvascular systems in rat brain. J Cereb Blood Flow Metab 1993;13:475–486.
28. Boxerman JL, Bandettini PA, Kwong KK, et al. The intravascular contribution to fMRI signal change: Monte Carlo modeling and diffusion-weighted studies in vivo. Magn Reson Med 1995;34:4–10.
29. Detre JA, Leigh JS, Williams DS, Koretsky AP. Perfusion imaging. Magn Reson Med 1992;23:37–45.
30. Ackerman JJ, Ewy CS, Kim S-G, Shalwitz RA. Deuterium magnetic resonance in vivo: the measurement of blood flow and tissue perfusion. Ann N Y Acad Sci 1987;508:89–98.
31. Williams DS, Detre JA, Leigh JS, Koretsky AP. Magnetic resonance imaging of perfusion using spin inversion of arterial water. Proc Natl Acad Sci USA 1992;89:212–216.
32. Duong TQ. In vivo MR measurements of regional arterial and venous blood volume fractions in intact rat brain. Magn Reson Med 2000;43:393–402.
33. Ulatowski JA, Oja JM, Suarez JI, Kauppinen RA, Traystman RJ, van Zijl PC. In vivo determination of absolute cerebral blood volume using hemoglobin as a natural contrast agent: an MRI study using altered arterial carbon dioxide tension. J Cereb Blood Flow Metab 1999;19:809–817.
34. Unger EC, Ugurbil K, Latchaw RE. Contrast agents for cerebral perfusion MR imaging. J Magn Reson Imaging 1994;4:235–242.

35. Østergaard L, Weisskoff RM, Chesler DA, Gyldensted C, Rosen BR. High resolution measurement of cerebral blood flow using intravascular tracer bolus passages. Part I: mathematical approach and statistical analysis. Magn Reson Med 1996;36:715–725.

36. Østergaard L, Sorensen AG, Kwong KK, Weisskoff RM, Gyldensted C, Rosen BR. High resolution measurement of cerebral blood flow using intravascular tracer bolus passages. Part II: experimental comparison and preliminary results. Magn Reson Med 1996;36: 726–736.

37. Thulborn KR, Waterton JC, Matthews PM, Radda GK. Oxygenation dependence of the transverse relaxation time of water protons in whole blood at high field. Biochim Biophys Acta 1982;714: 265–270.

38. Wright GA, Hu BS, Macovski A. Estimating oxygen saturation of blood in vivo with MR imaging at 1.5 T. J Magn Reson Imaging 1991;1:275–283.

39. Ye FQ, Allen PS. Relaxation enhancement of the transverse magnetization of water protons in paramagnetic suspensions of red blood cells. Magn Reson Med 1995;34:713–720.

40. Gillis P, Peto S, Moiny F, Mispelter J, Cuenod CA. Proton transverse nuclear magnetic relaxation in oxidized blood: a numerical approach. Magn Reson Med 1995;33:93–100.

41. Donahue KM, Weisskoff RM, Burstein D. Water diffusion and exchange as they influence contrast enhancement. J Magn Reson Imaging 1997;7:102–110.

42. Eichling JO, Raichle ME, Grubb Jr RL, Ter Pogossian MM. Evidence of the limitations of water as a freely diffusible tracer in brain of the rhesus monkey. Circ Res 1974;35:358–364.

43. Schwarzbauer C, Morrissey SP, Deichmann R, et al. Quantitative magnetic resonance imaging of capillary water permeability and regional blood volume with an intravascular MR contrast agent. Magn Reson Med 1997;37:769–777.

44. Boxerman JL, Hamberg LM, Rosen BR, Weisskoff RM. MR contrast due to intravascular magnetic susceptibility perturbations. Magn Reson Med 1995;34:555–566.

45. Ogawa S, Menon RS, Tank DW, et al. Functional brain mapping by blood oxygenation level-dependent contrast magnetic resonance imaging. A comparison of signal characteristics with a biophysical model. Biophys J 1993;64:803–812.

46. Kennan RP, Zhong J, Gore JC. Intravascular susceptibility contrast mechanisms in tissues. Magn Reson Med 1994;31:9–21.

47. Yablonskiy DA, Haacke EM. Theory of NMR signal behavior in magnetically inhomogeneous tissues: the static dephasing regime. Magn Reson Med 1994;32:749–763.

48. Weisskoff RM, Zuo CS, Boxerman JL, Rosen BR. Microscopic susceptibility variation and transverse relaxation: theory and experiment. Magn Reson Med 1994;31:601–610.

49. Bandettini PA, Wong EC. Effects of biophysical and physiological parameters on brain activation-induced R2* and R2 changes: simulations using a deterministic diffusion model. Int J Imaging Syst Technol 1995;6:133–152.

50. Kiselev VG, Posse S. Analytical theory of susceptibility induced NMR signal dephasing in a cerebrovascular network. Phys Rev Lett 1998;81:5696–5699.

51. Kiselev VG, Posse S. Analytical model of susceptibility-induced MR signal dephasing: effect of diffusion in a microvascular network. Magn Reson Med 1999;41:499–509.

52. Fisel CR, Ackerman JL, Buxton RB, et al. MR contrast due to microscopically heterogeneous magnetic susceptibility: numerical simulations and applications to cerebral physiology. Magn Reson Med 1991;17:336–347.

53. Stejskal EO, Tanner JE. Spin diffusion measurements: spin-echoes in the presence of a time-dependent field gradient. J Chem Phys 1965;42:288–292.

54. Prinster A, Pierpaoli C, Turner R, Jezzard P. Simultaneous measurement of ΔR2 and ΔR2* in cat brain during hypoxia and hypercapnia. Neuroimage 1997;6:191–200.

55. Tropres I, Grimault S, Vaeth A, et al. Vessel size imaging. Magn Reson Med 2001;in press.

56. Dennie J, Mandeville JB, Boxerman JL, Packard SD, Rosen BR, Weisskoff RM. NMR imaging of changes in vascular morphology due to tumor angiogenesis. Magn Reson Med 1998;40:793–799.

57. Donahue KM, Krouwer HG, Rand SD, et al. Utility of simultaneously acquired gradient-echo and spin-echo cerebral blood volume and morphology maps in brain tumor patients. Magn Reson Med 2000;43:845–853.

58. Dean BL, Lee C, Kirsch JE, Runge VM, Dempsey RM, Pettigrew LC. Cerebral hemodynamics and cerebral blood volume: MR assessment using gadolinium contrast agents and T1-weighted Turbo-FLASH imaging. Am J Neuroradiol 1992;13:39–48.

59. Thompson HK, Starmer CF, Whalen RE, McIntosh HD. Indicator transit time considered as a gamma-variate. Circ Res 1964;14: 502–515.

60. Meier P, Zierler KL. On the theory of the indicator-dilution method for measurement of blood flow and volume. J Appl Physiol 1954; 6:731–744.

61. Zierler KL. Theoretical basis of indicator dilution methods for measuring flow and volume. Circ Res 1962;10:393–407.

62. Rempp KA, Brix G, Wenz F, Beckers CR, Gückel F, Lorenz WJ. Quantification of regional cerebral blood flow and volume with dynamic susceptibility contrast enhanced MR imaging. Radiology 1994;193:637–641.

63. Bahn MM. A single-step method for estimation of local cerebral blood volume from susceptibility contrast MRI images. Magn Reson Med 1995;33:309–317.

64. Wirestam R, Andersson L, Ostergaard L, et al. Assessment of regional cerebral blood flow by dynamic susceptibility contrast MRI using different deconvolution techniques. Magn Reson Med 2000;43:691–700.

65. Smith AM, Grandin CB, Duprez T, Mataigne F, Cosnard G. Whole brain quantitative CBF and CBV measurements using MRI bolus tracking: comparison of methodologies. Magn Reson Med 2000; 43:559–564.

66. Vonken EPA, Beekman FJ, Bakker CJG, Viergever MA. Maximum likelihood estimation of cerebral blood flow in dynamic susceptibility contrast MRI. Magn Reson Med 1999;41:343–350.

67. Stehling MK, Brüning R, Rosen BR. Perfusion imaging with echo-planar imaging. In: Schmitt F, Stehling MK, Turner R, editors. Echo-planar imaging—theory, technique and application. Berlin: Springer; 1998. p 419–464.

68. Börnert P, Aldefeld B, Eggers H. Reversed spiral imaging for increased T2* contrast. In: Proceedings of the 8th Annual Meeting of ISMRM, Denver, 2000. p 303.

69. Boxerman JL, Rosen BR, Weisskoff RM. Signal-to-noise analysis of cerebral blood volume maps from dynamic NMR imaging studies. J Magn Reson Imaging 1997;7:528–537.

70. Heiland S, Kreibich W, Reith W, et al. Comparison of echo-planar sequences for perfusion-weighted MRI: which is best? Neuroradiology 1998;40:216–221.

71. Hou L, Yang Y, Mattay VS, Frank JA, Duyn JH. Optimization of fast acquisition methods for whole-brain relative cerebral blood volume (rCBV) mapping with susceptibility contrast agents. J Magn Reson Imaging 1999;9:233–239.

72. Oesterle C, Strohschein R, Köhler M, Schnell M, Hennig J. Benefits and pitfalls of keyhole imaging, especially in first-pass perfusion studies. J Magn Reson Imaging 2000;11:312–323.

73. Zigun JR, Frank JA, Barrios FA, et al. Measurement of brain activity with bolus administration of contrast agent and gradient-echo MR imaging. Radiology 1993;186:353–356.

74. Lewin JM, Kaufman MJ, Ross MH, et al. Sequential dynamic susceptibility contrast MR experiments in human brain: residual contrast agent effect, steady state, and hemodynamic perturbation. Magn Reson Med 1995;34:655–663.

75. Müller TB, Jones RA, Haraldseth O, Westby J, Unsgard G. Comparison of MR perfusion imaging and microsphere measurements of regional cerebral blood flow in a rat model of middle cerebral artery occlusion. Magn Reson Imaging 1996;14:1177–1183.

76. Petrella JR, DeCarli C, Dagli M, et al. Assessment of whole-brain vasodilatory capacity with acetazolamide challenge at 1.5 T using dynamic contrast imaging with frequency-shifted burst. Am J Neuroradiol 1997;18:1153–1161.

77. Østergaard L, Rabinov J, Rosen BR, Gyldensted C. Simultaneous blood flow, blood volume and blood brain barrier permeability mapping using Gd-based contrast agents. Proceedings of the 4th Annual Meeting of ISMRM, New York, 1996. p 1307.

78. Barbier EL, den Boer JA, Peters AR, Rozeboom AR, Sau J, Bonmartin A. A model of the dual effect of gadopentetate dimeglumine on dynamic brain MR images. J Magn Reson Imaging 1999; 10:242–253.

79. Haselhorst R, Kappos L, Bilecen D, et al. Dynamic susceptibility contrast MR imaging of plaque development in multiple sclerosis: application of an extended blood-brain barrier leakage correction. J Magn Reson Imaging 2000;11:495–505.

80. Hietschold V, Klengel S, Köhler K. Simultaneous dynamic measurement of tissue contrast enhancement and perfusion at 0.5 Tesla: method and postprocessing. New York: SMRM, twelfth annual meeting; 1993. p 619.

81. Miyati T, Banno T, Mase M, et al. Dual dynamic contrast-enhanced MR imaging. J Magn Reson Imaging 1997;7:230–235.

82. Su M-Y, Müller A, Lao X, Nalcioglu O. Tumor characterization with dynamic contrast enhanced MRI using MR contrast agents of various molecular weights. Magn Reson Med 1998;39:259–269.

83. Hackländer T, Reichenbach JR, Hofer M, Modder U. Measurement of cerebral blood volume via the relaxing effect of low-dose gadopentetate dimeglumine during bolus transit. Am J Neuroradiol 1996;17:821–830.

84. Hackländer T, Hofer M, Reichenbach JR, Rascher K, Fürst G, Mödder U. Cerebral blood volume maps with dynamic contrast-enhanced T1-weighted FLASH imaging: normal values and preliminary clinical results. J Comput Assist Tomogr 1996;20:532–539.

85. Hackländer T, Reichenbach JR, Modder U. Comparison of cerebral blood volume measurements using the T1 and T2* methods in normal human brains and brain tumors. J Comput Assist Tomogr 1997;21:857–866.

86. McKenzie CA, Pereira RS, Prato FS, Chen Z, Drost DJ. Improved contrast agent bolus tracking using T1 FARM. Magn Reson Med 1999;41:429–435.

87. Quast MJ, Wei J, Huang NC, et al. Perfusion deficit parallels exacerbation of cerebral ischemia/reperfusion injury in hyperglycemic rats. J Cereb Blood Flow Metab 1997;17:553–559.

88. Belliveau JW, Kennedy DN, McKinstry RC, et al. Functional mapping of the human visual cortex by magnetic resonance imaging. Science 1991;254:716–719.

89. Maeda M, Itoh S, Kimura H, et al. Tumor vascularity in the brain: evaluation with dynamic susceptibility-contrast MR imaging. Radiology 1993;189:233–238.

90. Warach S, Dashe JF, Edelman RR. Clinical outcome in ischemic stroke predicted by early diffusion-weighted and perfusion magnetic resonance imaging: a preliminary analysis. J Cereb Blood Flow Metab 1996;16:53–59.

91. Reith W, Heiland S, Erb G, Benner T, Forsting M, Sartor K. Dynamic contrast-enhanced T2*-weighted MRI in patients with cerebrovascular disease. Neuroradiology 1997;39:250–257.

92. Baird AE, Warach S. Imaging developing brain infarction. Curr Opin Neurol 1999;12:65–71.

93. Cha S, Knopp EA, Johnson G, et al. Dynamic contrast-enhanced T2-weighted MR imaging of recurrent malignant gliomas treated with thalidomide and carboplatin. AJNR Am J Neuroradiol 2000; 21:881–890.

94. Aronen HJ, Gazit IE, Louis DN, et al. Cerebral blood volume maps of gliomas: comparison with tumor grade and histologic findings. Radiology 1994;191:41–51.

95. Siegal T, Rubinstein R, Tzuk-Shina T, Gomori JM. Utility of relative cerebral blood volume mapping derived from perfusion magnetic resonance imaging in the routine follow up of brain tumors. J Neurosurg 1997;86:22–27.

96. Ostergaard L, Hochberg FH, Rabinov JD, et al. Early changes measured by magnetic resonance imaging in cerebral blood flow, blood volume, and blood-brain barrier permeability following dexamethasone treatment in patients with brain tumors. J Neurosurg 1999;90:300–305.

97. Sunshine JL, Tarr RW, Lanzieri CF, Landis DM, Selman WR, Lewin JS. Hyperacute stroke: ultrafast MR imaging to triage patients prior to therapy. Radiology 1999;212:325–332.

98. Sorensen AG, Copen WA, Ostergaard L, et al. Hyperacute stroke: simultaneous measurement of relative cerebral blood volume, relative cerebral blood flow, and mean tissue transit time. Radiology 1999;210:519–527.

99. Liu Y, Karonen JO, Vanninen RL, et al. Cerebral hemodynamics in human acute ischemic stroke: a study with diffusion- and perfusion-weighted magnetic resonance imaging and SPECT. J Cereb Blood Flow Metab 2000;20:910–920.

100. Weisskoff RM, Chesler DA, Boxerman JL, Rosen BR. Pitfalls in MR measurement of tissue blood flow with intravascular tracers: which mean transit time? Magn Reson Med 1993;29:553–558.

101. Moody AR, Martel A, Kenton A, et al. Contrast-reduced imaging of tissue concentration and arterial level (CRITICAL) for assessment of cerebral hemodynamics in acute stroke by magnetic resonance. Invest Radiol 2000;35:401–411.

102. Enochs WS, Harsh G, Hochberg F, Weissleder R. Improved delineation of human brain tumors on MR images using a long-circulating, superparamagnetic iron oxide agent. J Magn Reson Imaging 1999;9:228–232.

103. Moseley ME, Chew WM, White DL, et al. Hypercarbia-induced changes in cerebral blood volume in the cat: a 1H MRI and intravascular contrast agent study. Magn Reson Med 1992;23:21–30.

104. Kuppusamy K, Lin W, Cizek GR, Haacke EM. In vivo regional cerebral blood volume: quantitative assessment with 3D T1-weighted pre- and postcontrast MR imaging. Radiology 1996;201: 106–112.

105. Lin W, Celik A, Paczynski RP. Regional cerebral blood volume: a comparison of the dynamic imaging and the steady state methods. J Magn Reson Imaging 1999;9:44–52.

106. Hamberg LM, Boccalini P, Stranjalis G, et al. Continuous assessment of relative cerebral blood volume in transient ischemia using steady state susceptibility-contrast MRI. Magn Reson Med 1996; 35:168–173.

107. Jones RA, Haraldseth O, Baptista AM, Muller TB, Oksendal AN. A study of the contribution of changes in the cerebral blood volume to the haemodynamic response to anoxia in rat brain. NMR Biomed 1997;10:59–66.

108. Lin W, Paczynski RP, Kuppusamy K, Hsu CY, Haacke EM. Quantitative measurements of regional cerebral blood volume using MRI in rats: effects of arterial carbon dioxide tension and mannitol. Magn Reson Med 1997;38:420–428.

109. Payen JF, Vath A, Koenigsberg B, Bourlier V, Decorps M. Regional cerebral plasma volume response to carbon dioxide using magnetic resonance imaging. Anesthesiology 1998;88:984–992.

110. Speck O, Chang L, Itti L, Itti E, Ernst T. Comparison of static and dynamic MRI techniques for the measurement of regional cerebral blood volume. Magn Reson Med 1999;41:1264–1268.

111. Lin W, Celik A, Paczynski RP, Hsu CY, Powers WJ. Quantitative magnetic resonance imaging in experimental hypercapnia: improvement in the relation between changes in brain R2 and the oxygen saturation of venous blood after correction for changes in cerebral blood volume. J Cereb Blood Flow Metab 1999;19:853–862.

112. Chen Q, Andersen AH, Zhang Z, Ovadia A, Gash DM, Avison MJ. Mapping drug-induced changes in cerebral R2* by multiple gradient recalled echo functional MRI. Magn Reson Imaging 1996; 14:469–476.

113. Payen J-F, Briot E, Tropres I, Julien-Dolbec C, Montigon O, Décorps M. Regional cerebral blood volume response to hypocapnia using susceptibility contrast MRI. NMR Biomed 2000;13:384–391.

114. Scheffler K, Seifritz E, Haselhorst R, Bilecen D. Titration of the BOLD effect: separation and quantitation of blood volume and oxygenation changes in the human cerebral cortex during neuronal activation and ferumoxide infusion. Magn Reson Med 1999; 42:829–836.

115. Abramovitch R, Frenkiel D, Neeman M. Analysis of subcutaneous angiogenesis by gradient echo magnetic resonance imaging. Magn Reson Med 1998;39:813–824.

116. Le Duc G, Péoc'h M, Remy C, et al. Use of T2-weighted susceptibility contrast MRI for mapping the blood volume in the glioma-bearing rat brain. Magn Reson Med 1999;42:754–761.

117. Simonsen CZ, Ostergaard L, Vestergaard-Poulsen P, Rohl L, Bjornerud A, Gyldensted C. CBF and CBV measurements by USPIO bolus tracking: reproducibility and comparison with Gd-based values. J Magn Reson Imaging 1999;9:342–347.

118. Zaharchuk G, Bogdanov AAJ, Marota JJ, et al. Continuous assessment of perfusion by tagging including volume and water extraction (CAPTIVE): a steady-state contrast agent technique for measuring blood flow, relative blood volume fraction, and the water extraction fraction. Magn Reson Med 1998;40:666–678.

119. Zaharchuk G, Mandeville JB, Bogdanov Jr AA, Weissleder R, Rosen BR, Marota JJ. Cerebrovascular dynamics of autoregulation and hypoperfusion. An MRI study of CBF and changes in total and microvascular cerebral blood volume during hemorrhagic hypotension. Stroke 1999;30:2197–2204.

120. Landau WM, Freygang WAJ, Rowland LP, Sokoloff L, Kety SS. The local circulation of the living brain: values in the unanesthetized and anesthetized cat. Trans Am Neurol Assoc 1955;80:125–129.

121. Sakurada O, Kennedy C, Jehle J, Brown JD, Carbin GL, Sokoloff L. Measurement of local cerebral blood flow with iodo[^{14}C]antipyrine. Am J Physiol 1978;234:H59–H66.

122. Glass HI, Harper AM. Measurement of regional blood flow in cerebral cortex of man through the intact skull. Brit M J 1963;1: 593.

123. Kanno I, Uemura K, Miura S, Miura Y. HEADTOME: a hybrid emission tomograph for single photon and positron emission imaging of the brain. J Comput Assist Tomogr 1981;5:216–226.

124. Bruyant P, Sau J, Mallet JJ, Bonmartin A. Regional cerebral blood flow determination using 133Xe and a standard rotating gamma-camera. Comput Biol Med 1998;28:27–45.

125. Veall N, Mallet BL. The two-compartment model using ^{133}Xe inhalation and external counting. Acta Physiol Scand 1965;14:83–84.

126. Raichle ME. Measurement of local cerebral blood flow and metabolism in man with positron emission tomography. Fed Proc 1981; 40:2331–2334.

127. Raichle ME, Martin WR, Herscovitch P, Mintun MA, Markham J. Brain blood flow measured with intravenous H2(15)O. II. Implementation and validation. J Nucl Med 1983;24:790–798.

128. Powers WJ, Grubb Jr RL, Darriet D, Raichle ME. Cerebral blood flow and cerebral metabolic rate of oxygen requirements for cerebral function and viability in humans. J Cereb Blood Flow Metab 1985;5:600–608.

129. Kety SS, Schmidt CF. The determination of cerebral blood flow in man by use of nitrous oxide in low concentrations. Am J Physiol 1945;143:53–66.

130. Ackerman JJ, Ewy CS, Becker NN, Shalwitz RA. Deuterium nuclear magnetic resonance measurements of blood flow and tissue perfusion employing 2H2O as a freely diffusible tracer. Proc Natl Acad Sci USA 1987;84:4099–4102.

131. Ross BD, Mitchell SL, Merkle H, Garwood M. In vivo 31P and 2H NMR studies of rat brain tumor pH and blood flow during acute hyperglycemia: differential effects between subcutaneous and intracerebral locations. Magn Reson Med 1989;12:219–234.

132. Kim S-G, Ackerman JJ. Quantification of regional blood flow by monitoring of exogenous tracer via nuclear magnetic resonance spectroscopy. Magn Reson Med 1990;14:266–282.

133. Detre JA, Subramanian VH, Mitchell MD, et al. Measurement of regional cerebral blood flow in cat brain using intracarotid 2H2O and 2H NMR imaging. Magn Reson Med 1990;14:389–395.

134. Corbett RJ, Laptook AR, Olivares E. Simultaneous measurement of cerebral blood flow and energy metabolites in piglets using deuterium and phosphorus nuclear magnetic resonance. J Cereb Blood Flow Metab 1991;11:55–65.

135. Eleff SM, Schnall MD, Ligetti L, et al. Concurrent measurements of cerebral blood flow, sodium, lactate, and high-energy phosphate metabolism using 19F, 23Na, 1H, and 31P nuclear magnetic resonance spectroscopy. Magn Reson Med 1988;7:412–424.

136. Rudin M, Sauter A. Non-invasive determination of cerebral blood flow changes by 19F NMR spectroscopy. NMR Biomed 1989;2:98–103.

137. Ewing JR, Branch CA, Helpern JA, Smith MB, Butt SM, Welch KM. Cerebral blood flow measured by NMR indicator dilution in cats. Stroke 1989;20:259–267.

138. Branch CA, Ewing JR, Fagan SC, Goldberg DA, Welch KM. Acute toxicity of a nuclear magnetic resonance cerebral blood flow indicator in cats. Stroke 1990;21:1172–1177.

139. Pekar J, Ligeti L, Sinnwell TM, Moonen CT, Frank JA, McLaughlin AC. 19F magnetic resonance imaging of cerebral blood flow with 0.4-cc resolution. J Cereb Blood Flow Metab 1994;14:656–663.

140. Barranco D, Sutton LN, Florin S, et al. Use of 19F NMR spectroscopy for measurement of cerebral blood flow: a comparative study using microspheres. J Cereb Blood Flow Metab 1989;9:886–891.

141. Mateescu GD, Yvars GM, Pazara DI, et al. Oxygen-17: a physiological, biochemical and anatomical MRI contrast agent. San Francisco: SMRM, seventh annual meeting; 1988. p 600.

142. Hopkins AL, Barr RG. Oxygen-17 compounds as potential NMR T2 contrast agents: enrichment effects of H2(17)O on protein solutions and living tissues. Magn Reson Med 1987;4:399–403.

143. Pekar J, Ligeti L, Ruttner Z, et al. In vivo measurement of cerebral oxygen consumption and blood flow using 17O magnetic resonance imaging. Magn Reson Med 1991;21:313–319.

144. Arai T, Nakao S, Mori K, et al. Cerebral oxygen utilization analyzed by the use of oxygen-17 and its nuclear magnetic resonance. Biochem Biophys Res Commun 1990;169:153–158.

145. Arai T, Mori K, Nakao S, et al. In vivo oxygen-17 nuclear magnetic resonance for the estimation of cerebral blood flow and oxygen consumption. Biochem Biophys Res Commun 1991;179:954–961.

146. Chiarotti G, Cristiani G, Giuletto L. Proton relaxation in pure liquids and in liquids containing paramagnetic gases in solution. Nuovo Cim 1955;1:863–873.

147. Meiboom S. Nuclear magnetic resonance study of the proton transfer in water. J Chem Phys 1961;34:375–388.

148. Kwong KK, Hopkins AL, Belliveau JW, et al. Proton NMR imaging of cerebral blood flow using H2(17)O. Magn Reson Med 1991;22: 154–158.

149. Arai T, Nakao S, Morikawa S, et al. Measurement of local cerebral blood flow by magnetic resonance imaging: in vivo autoradiographic strategy using 17O-labeled water. Brain Res Bull 1998; 45:451–456.

150. Swanson SD, Rosen MS, Agranoff BW, Coulter KP, Welsh RC, Chupp TE. Brain MRI with laser-polarized 129Xe. Magn Reson Med 1997;38:695–698.

151. Kwong KK, Belliveau JW, Chesler DA, et al. Dynamic magnetic resonance imaging of human brain activity during primary sensory stimulation. Proc Natl Acad Sci USA 1992;89:5675–5679.

152. Wolff SD, Balaban RS. Magnetization transfer contrast (MTC) and tissue water proton relaxation in vivo. Magn Reson Med 1989;10: 135–144.

153. Calamante F, Thomas DL, Pell GS, Wiersma J, Turner R. Measuring cerebral blood flow using magnetic resonance imaging techniques. J Cereb Blood Flow Metab 1999;19:701–735.

154. Buxton RB, Frank LR, Wong EC, Siewert B, Warach S, Edelman RR. A general kinetic model for quantitative perfusion imaging with arterial spin labeling. Magn Reson Med 1998;40:383–396.

155. Herscovitch P, Raichle ME. What is the correct value for the brain—blood partition coefficient for water? J Cereb Blood Flow Metab 1985;5:65–69.

156. Roberts DA, Rizi R, Lenkinski RE, Leigh Jr JS. Magnetic resonance imaging of the brain-blood partition coefficient for water: application to spin-tagging measurement of perfusion. J Magn Reson Imaging 1996;6:363–366.

157. Williams DS, Grandis DJ, Zhang W, Koretsky AP. Magnetic resonance imaging of perfusion in the isolated rat heart using spin inversion of arterial water. Magn Reson Med 1993;30:361–365.

158. Dixon WT, Du LN, Faul DD, Gado M, Rossnick S. Projection angiograms of blood labeled by adiabatic fast passage. Magn Reson Med 1986;3:454–462.

159. Abragam A. Cours sur les phénomènes liés à la résonance magnétique. Saclay: Centre d'étude nucléaires de Saclay; 1955. 399 p.

160. Zhang W, Williams DS, Koretsky AP. Measurement of rat brain perfusion by NMR using spin labeling of arterial water: in vivo determination of the degree of spin labeling. Magn Reson Med 1993;29:416–421.

161. Zhang W, Williams DS, Detre JA, Koretsky AP. Measurement of brain perfusion by volume-localized NMR spectroscopy using inversion of arterial water spins: accounting for transit time and cross-relaxation. Magn Reson Med 1992;25:362–371.

162. Maccotta L, Detre JA, Alsop DC. The efficiency of adiabatic inversion for perfusion imaging by arterial spin labeling. NMR Biomed 1997;10:216–221.

163. Marro KI, Hayes CE, Kushmerick MJ. A model of the inversion process in an arterial inversion experiment. NMR Biomed 1997; 10:324–332.

164. McLaughlin AC, Ye FQ, Pekar J, Santha AK, Frank JA. Effect of magnetization transfer on the measurement of cerebral blood flow using steady-state arterial spin tagging approaches: a theoretical investigation. Magn Reson Med 1997;37:501–510.

165. Zhang W, Silva AC, Williams DS, Koretsky AP. NMR measurement of perfusion using arterial spin labeling without saturation of macromolecular spins. Magn Reson Med 1995;33:370–376.

166. Silva AC, Zhang W, Williams DS, Koretsky AP. Estimation of water extraction fractions in rat brain using magnetic resonance measurement of perfusion with arterial spin labeling. Magn Reson Med 1997;38:35–58.

167. Roberts DA, Detre JA, Bolinger L, Insko EK, Leigh Jr JS. Quantitative magnetic resonance imaging of human brain perfusion at 1.5 T using steady-state inversion of arterial water. Proc Natl Acad Sci USA 1994;91:33–37.

168. Alsop DC, Detre JA. Multisection cerebral blood flow MR imaging with continuous arterial spin labeling. Radiology 1998;208:410–416.

169. Talagala SL, Barbier EL, Williams DS, Silva AC, Koretsky AP. Multi-slice perfusion MRI using continuous arterial water labeling controling for MT effects with simultaneous proximal and distal RF irradiation. In: Proceedings of the 6th Annual Meeting of ISMRM, Sydney, 1998. p 381.

170. Silva AC, Zhang W, Williams DS, Koretsky AP. Multi-slice MRI of rat brain perfusion during amphetamine stimulation using arterial spin labeling. Magn Reson Med 1995;33:209–214.

171. Zaharchuk G, Ledden PJ, Kwong KK, Reese TG, Rosen BR, Wald LL. Multislice perfusion and perfusion territory imaging in humans with separate label and image coils. Magn Reson Med 1999; 41:1093–1098.

172. Lei H, Peeling J. A strategy to optimize the signal-to-noise ratio in one-coil arterial spin tagging perfusion imaging. Magn Reson Med 1999;41:563–568.

173. Zhang W. A quantitative analysis of alternated line scanning in k space and its application in MRI of regional tissue perfusion by arterial spin labeling. J Magn Reson B 1995;107:165–171.

174. Pekar J, Jezzard P, Roberts DA, Leigh JS, Frank JA, McLaughlin AC. Perfusion imaging with compensation for asymetric magnetization transfer effects. Magn Reson Med 1996;35:70–79.

175. Ye FQ, Mattay VS, Jezzard P, Frank JA, Weinberger DR, McLaughlin AC. Correction for vascular artifacts in cerebral blood flow values measured by using arterial spin tagging techniques. Magn Reson Med 1997;37:226–237.

176. Le Bihan D, Breton E, Lallemand D, Aubin ML, Vignaud J, Laval-Jeantet M. Separation of diffusion and perfusion in intravoxel incoherent motion MR imaging. Radiology 1988;168:497–505.

177. Henkelman RM, Neil JJ, Xiang Q-S. A quantitative interpretation of IVIM measurements of vascular perfusion in the rat brain. Magn Reson Med 1994;32:464–469.

178. Kim S-G. Quantification of relative cerebral blood flow change by flow-sensitive alternating inversion recovery (FAIR) technique: application to functional mapping. Magn Reson Med 1995;34:293–301.

179. Alsop DC, Detre JA. Reduced transit-time sensitivity in noninvasive magnetic resonance imaging of human cerebral blood flow. J Cereb Blood Flow Metab 1996;16:1236–1249.

180. Kwong KK, Chesler DA, Weisskoff RM, et al. MR perfusion studies with T_1-weighted echo-planar imaging. Magn Reson Med 1995;34: 878–887.

181. Schwarzbauer C, Morrissey SP, Haase A. Quantitative magnetic resonance imaging of perfusion using magnetic labeling of water proton spins within the detection slice. Magn Reson Med 1996; 35:540–546.

182. Helpern JA, Branch CA, Yongbi MN, Huang NC. Perfusion imaging by un-inverted flow-sensitive alternating inversion recovery (UNFAIR). Magn Reson Imaging 1997;15:135–139.

183. Schwarzbauer C, Heinke W. BASE imaging: a new spin labeling technique for measuring absolute perfusion changes. Magn Reson Med 1998;39:717–722.

184. Mai VM, Berr SS. MR perfusion imaging of pulmonary parenchyma using pulsed arterial spin labeling techniques: FAIRER and FAIR. J Magn Reson Imaging 1999;9:483–487.

185. Zhou J, Mori S, van Zijl PC. FAIR excluding radiation damping (FAIRER). Magn Reson Med 1998;40:712–719.

186. Edelman RR, Siewert B, Darby DG, et al. Qualitative mapping of cerebral blood flow and functional localization with echo-planar imaging and signal targeting with alternating radio frequency. Radiology 1994;192:513–520.

187. Chen Q, Siewert B, Bly BM, Warach S, Edelman RR. STAR-HASTE: perfusion imaging without magnetic susceptibility artifact. Magn Reson Med 1997;38:404–408.

188. Edelman RR, Chen Q. EPISTAR MRI: multislice mapping of cerebral blood flow. Magn Reson Med 1998;40:800–805.

189. Golay X, Stuber M, Pruessmann KP, Meier D, Boesiger P. Transfer insensitive labeling technique (TILT): application to multislice functional perfusion imaging. J Magn Reson Imaging 1999;9: 454–461.

190. Wong EC, Buxton RB, Frank LR. Implementation of quantitative perfusion imaging techniques for functional brain mapping using pulsed arterial spin labeling. NMR Biomed 1997;10:237–249.

191. Wong EC, Buxton RB, Frank LR. Quantitative imaging of perfusion using a single subtraction (QUIPSS and QUIPSS II). Magn Reson Med 1998;39:702–708.

192. Luh WM, Wong EC, Bandettini PA, Hyde JS. QUIPSS II with thin-slice TI1 periodic saturation: a method for improving accuracy of quantitative perfusion imaging using pulsed arterial spin labeling. Magn Reson Med 1999;41:1246–1254.

193. Calamante F, Williams SR, van Bruggen N, Kwong KK, Turner R. A model for quantification of perfusion in pulsed labeling techniques. NMR Biomed 1996;9:79–83.

194. Kao YH, Wan X, MacFall JR. Simultaneous multislice acquisition with arterial-flow tagging (SMART) using echo planar imaging (EPI). Magn Reson Med 1998;39:662–665.

195. Yang Y, Frank JA, Hou L, Ye FQ, McLaughlin AC, Duyn JH. Multislice imaging of quantitative cerebral perfusion with pulsed arterial spin labeling. Magn Reson Med 1998;39:825–832.

196. Yongbi MN, Branch CA, Helpern JA. Perfusion imaging using FOCI RF pulses. Magn Reson Med 1998;40:983–943.

197. Ye FQ, Frank JA, Weinberger DR, McLaughlin AC. Noise reduction in 3D perfusion imaging by attenuating the static signal in arterial spin tagging (ASSIST). Magn Reson Med 2000;44:92–100.

198. Dixon WT, Sardashti M, Castillo M, Stomp GP. Multiple inversion recovery reduces static tissue signal in angiograms. Magn Reson Med 1991;18:257–268.

199. Barbier EL, Silva AC, Kim HJ, Williams DS, Koretsky AP. Perfusion analysis using dynamic arterial spin labeling (DASL). Magn Reson Med 1999;41:299–308.

200. Barbier EL, Silva AC, Kim S-G, Sau J, Mallet J-J, Koretsky AP. Simultaneous measurement of perfusion and vascular blood fraction using dynamic arterial spin labeling (DASL). In: Proceedings of the 7th Annual Meeting of ISMRM, Philadelphia, 1999. p 1744.

201. Blamire AM, Styles P. Spin echo entrapped perfusion image (SEEPAGE). A nonsubtraction method for direct imaging of perfusion. Magn Reson Med 2000;43:701–704.

202. Duyn J, Tan CX, van der Veen JW, et al. Perfusion-weighted "single-trial" fMRI. In: Proceedings of the 8th Annual Meeting of ISMRM, Denver, 2000. p 55.

203. Silva AC, Williams DS, Koretsky AP. Evidence for the exchange of arterial spin-labeled water with tissue water in rat brain from diffusion sensitized measurements of perfusion. Magn Reson Med 1997;38:232–237.

204. St. Lawrence KS, Frank JA, McLaughlin AC. Effect of restricted water exchange on cerebral blood flow values calculated with arterial spin tagging: a theoretical investigation. Magn Reson Med 2000;44:440–449.

205. Ewing JR, Fenstermacher JD. The single-coil arterial spin-tagging experiment for estimating cerebral blood flow as viewed from the capillary. What is the effective T1 of the experiment? In: Proceedings of the 7th Annual Meeting of ISMRM, Philadelphia, 1999. p 1846.

206. Takagi S, Ehara K, Finn RD. Water extraction fraction and permeability-surface product after intravenous injection in rats. Stroke 1987;18:177–183.

207. Go KG, Lammertsma AA, Paans AM, Vaalburg W, Woldring MG. Extraction of water labeled with oxygen 15 during single-capillary transit. Influence of blood pressure, osmolarity, and blood-brain barrier damage. Arch Neurol 1981;38:581–584.

208. Hendrich KS, Kochanek PM, Williams DS, Schiding JK, Marion DW, Ho C. Early perfusion after controlled cortical impact in rats: quantification by arterial spin-labeled MRI and the influence of spin-lattice relaxation time heterogeneity. Magn Reson Med 1999; 42:673–681.

209. Ogawa S, Lee TM, Kay AR, Tank DW. Brain magnetic resonance imaging with contrast dependent on blood oxygenation. Proc Natl Acad Sci USA 1990;87:9868–9872.

210. Walsh EG, Minematsu K, Leppo J, Moore SC. Radioactive microsphere validation of a volume localized continuous saturation perfusion measurement. Magn Reson Med 1994;31:147–153.

211. Pell GS, Proctor E, Thomas DL, Busza AL, Ordidge RJ. Validation of the FAIR technique of perfusion quantification with hydrogen clearance. In: Proceedings of the 7th Annual Meeting of ISMRM, Philadelphia, 1999. p 599.

212. Ewing JR, Wei L, Knight R, Nagaraja TN, Fenstermacher JD. A direct comparison between MRI arterial spin-tagging and quantitative autoradiography for measured cerebral blood flow in rats with experimental cerebral ischemia. Copenhagen: Brain '99, 19th annual meeting; 1999. p 595.

213. Hoehn M, Kruger K, Busch E, Franke C. Validation of arterial spin tagging perfusion using MR imaging: correlation with autoradiographic CBF data. In: Proceedings of the 7th Annual Meeting of ISMRM, Philadelphia, 1999. p 1843.

214. Ye FQ, Berman KF, Ellmore T, et al. H215O PET validation of steady-state arterial spin tagging cerebral blood flow measurements in humans. Magn Reson Med 2000;in press.

215. Tsekos NV, Zhang F, Merkle H, Nagayama M, Iadecola C, Kim S-G. Quantitative measurements of cerebral blood flow in rats using the FAIR technique: correlation with previous iodoantipyrine autoradiographic studies. Magn Reson Med 1998;39:564–573.

216. Detre JA, Alsop DC. Perfusion magnetic resonance imaging with continuous arterial spin labeling: methods and clinical applications in the central nervous system. Eur J Radiol 1999;30:115–124.

217. Kerskens CM, Hoehn-Berlage M, Schmitz B, et al. Ultrafast perfusion-weighted MRI of functional brain activation in rats during forepaw stimulation: comparison with T2-weighted MRI. NMR Biomed 1996;9:20–23.

218. Ye FQ, Smith AM, Yang Y, et al. Quantitation of regional cerebral blood flow increases during motor activation: a steady-state arterial spin tagging study. Neuroimage 1997;6:104–112.

219. Li TQ, Moseley ME, Glover G. A FAIR study of motor cortex activation under normo- and hypercapnia induced by breath challenge. Neuroimage 1999;10:562–569.

220. Luh WM, Wong EC, Bandettini PA, Ward BD, Hyde JS. Comparison of simultaneously measured perfusion and BOLD signal increases during brain activation with T1-based tissue identification. Magn Reson Med 2000;44:137–143.

221. Kim SG, Ugurbil K. Comparison of blood oxygenation and cerebral blood flow effects in fMRI: estimation of relative oxygen consumption change. Magn Reson Med 1997;38:59–65.

222. Zhu XH, Kim SG, Andersen P, Ogawa S, Ugurbil K, Chen W. Simultaneous oxygenation and perfusion imaging study of functional activity in primary visual cortex at different visual stimulation frequency: quantitative correlation between BOLD and CBF changes. Magn Reson Med 1998;40:703–711.

223. Silva AC, Lee SP, Yang G, Iadecola C. Simultaneous blood oxygenation level-dependent and cerebral blood flow functional magnetic resonance imaging during forepaw stimulation in the rat. J Cereb Blood Flow Metab 1999;19:871–879.

224. Gonzalez-At JB, Alsop DC, Detre JA. Cerebral perfusion and arterial transit time changes during task activation determined with continuous arterial spin labeling. Magn Reson Med 2000;43:739–746.

225. Belle V, Delon-martin C, Massarelli R, et al. Intracranial gradient-echo and spin-echo functional MR angiography in humans. Radiology 1995;195:739–746.

226. Forman SD, Silva AC, Dedousis N, Barbier EL, Fernstrom JD, Koretsky AP. Simultaneous glutamate and perfusion fMRI responses to regional brain stimulation. J Cereb Blood Flow Metab 1998;18:1064–1070.

227. Forbes ML, Hendrich KS, Kochanek PM, et al. Assessment of cerebral blood flow and CO2 reactivity after controlled cortical impact by perfusion magnetic resonance imaging using arterial spin-labeling in rats. J Cereb Blood Flow Metab 1997;17:865–874.

228. Hendrich KS, Kochanek PM, Melick JA, et al. Characterization of cerebral blood flow during anesthesia with fentanyl, isoflurane, or pentobarbital in normal rats. In: Proceedings of the 8th Annual Meeting of ISMRM, Denver, 2000. p 1277.

229. Li TQ, Chen ZG, Østergaard L, Hindmarsh T, Moseley ME. Quantification of cerebral blood flow by bolus tracking and artery spin tagging methods. Magn Reson Imaging 2000;18:503–512.

230. Jiang Q, Zhang ZG, Chopp M, et al. Temporal evolution and spatial distribution of the diffusion constant of water in rat brain after transient middle cerebral artery occlusion. J Neurol Sci 1993;120:123–130.

231. Jiang Q, Chopp M, Zhang ZG, et al. The effect of hypothermia on transient focal ischemia in rat brain evaluated by diffusion- and perfusion-weighted NMR imaging. J Cereb Blood Flow Metab 1994;14:732–741.

232. Busch E, Kruger K, Allegrini PR, et al. Reperfusion after thrombolytic therapy of embolic stroke in the rat: magnetic resonance and biochemical imaging. J Cereb Blood Flow Metab 1998;18:407–418.

233. Jiang Q, Zhang ZG, Zhang RL, et al. Diffusion, perfusion, and T2 magnetic resonance imaging of anti-intercellular adhesion molecule 1 antibody treatment of transient middle cerebral artery occlusion in rat. Brain Res 1998;788:191–201.

234. Calamante F, Lythgoe MF, Pell GS, et al. Early changes in water diffusion, perfusion, T1, and T2 during focal cerebral ischemia in the rat studied at 8.5 T. Magn Reson Med 1999;41:479–485.

235. Siewert B, Schlaug G, Edelman RR, Warach S. Comparison of EPISTAR and T2*-weighted gadolinium-enhanced perfusion imaging in patients with acute cerebral ischemia. Neurology 1997;48:673–679.

236. Detre JA, Samuels OB, Alsop DC, Gonzalez-At JB, Kasner SE, Raps EC. Noninvasive magnetic resonance imaging evaluation of cerebral blood flow with acetazolamide challenge in patients with cerebrovascular stenosis. J Magn Reson Imaging 1999;10:870–875.

237. Chalela JA, Alsop DC, Gonzalez-Atavales JB, Maldjian JA, Kasner SE, Detre JA. Magnetic resonance perfusion imaging in acute ischemic stroke using continuous arterial spin labeling. Stroke 2000;31:680–687.

238. Alsop DC, Detre JA, Grossman M. Assessment of cerebral blood flow in Alzheimer's disease by spin-labeled magnetic resonance imaging. Ann Neurol 2000;47:93–100.

239. Gaa J, Warach S, Wen P, Thangaraj V, Wielopolski ERR. Noninvasive perfusion imaging of human brain tumors with EPISTAR. Eur Radiol 1996;6:518–512.

240. Brown SL, Ewing JR, Kolozsvary A, Butt S, Cao Y, Kim JH. Magnetic resonance imaging of perfusion in rat cerebral 9L tumor after nicotinamide administration. Int J Radiat Oncol Biol Phys 1999;43:627–633.

241. Silva AC, Kim SG, Garwood M. Imaging blood flow in brain tumors using arterial spin labeling. Magn Reson Med 2000;44:169–173.

242. Sakai F, Nakazawa K, Tazaki Y, et al. Regional cerebral blood volume and hematocrit measured in normal human volunteers by single-photon emission computed tomography. J Cereb Blood Flow Metab 1985;5:207–213.

243. Archer DP, Labrecque P, Tyler JL, et al. Measurement of cerebral blood flow and volume with positron emission tomography during isoflurane administration in the hypocapnic baboon. Anesthesiology 1990;72:1031–1037.

244. Shockley RP, LaManna JC. Determination of rat cerebral cortical blood volume changes by capillary mean transit time analysis during hypoxia, hypercapnia and hyperventilation. Brain Res 1988;454:170–178.

245. Todd MM, Weeks JB, Warner DS. Microwave fixation for the determination of cerebral blood volume in rats. J Cereb Blood Flow Metab 1993;13:328–336.

246. Martin AJ, Friston KJ, Colebatch JG, Frackowiak RS. Decreases in regional cerebral blood flow with normal aging. J Cereb Blood Flow Metab 1991;11:684–689.